The PhysIO Toolbox for Modeling Physiological Noise in fMRI Data

Lars Kasper [a,b,∗], Steffen Bollmann [c], Andreea O. Diaconescu [a], Chloe Hutton [d],
Jakob Heinzle [a], Sandra Iglesias [a], Tobias U. Hauser [d,e], Miriam Sebold [f],
Zina-Mary Manjaly [g], Klaas P. Pruessmann [b], Klaas E. Stephan [a,d,h]

[a] Translational Neuromodeling Unit (TNU), Institute for Biomedical Engineering, University of Zurich and ETH Zurich, Wilfriedstrasse 6, 8032 Zurich, Switzerland
[b] Institute for Biomedical Engineering, ETH Zurich and University of Zurich, Gloriastrasse 35, 8092 Zurich, Switzerland
[c] Centre for Advanced Imaging, University of Queensland, Brisbane, QLD, 4072, Australia
[d] Wellcome Trust Centre for Neuroimaging, University College London, London WC1N 3BG, UK
[e] Max Planck University College London Centre for Computational Psychiatry and Ageing Research, London WC1 B 5EH, UK
[f] Department of Psychiatry and Psychotherapy, Campus Mitte, Charité Universitätsmedizin, 10117 Berlin, Germany
[g] Department of Neurology, Schulthess Clinic, 8008 Zurich, Switzerland
[h] Max Planck Institute for Metabolism Research, 50931 Cologne, Germany

HIGHLIGHTS

- A Toolbox to integrate preprocessing of physiological data and fMRI noise modeling.
- Robust preprocessing via iterative peak detection, shown for noisy data and patients.
- Flexible support of peripheral data formats and noise models (RETROICOR, RVHRCOR).
- Fully automated noise correction and performance assessment for group studies.
- Integration in fMRI pre-processing pipelines as SPM Toolbox (Batch Editor GUI).

GRAPHICAL ABSTRACT
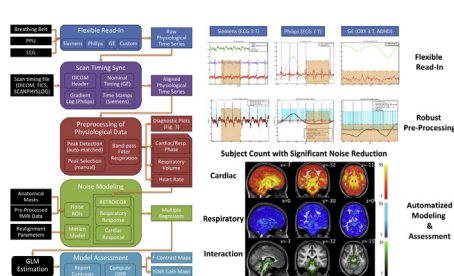
ARTICLE INFO

ABSTRACT

Background: Physiological noise is one of the major confounds for fMRI. A common class of correction methods model noise from peripheral measures, such as ECGs or pneumatic belts. However, physiological noise correction has not emerged as a standard preprocessing step for fMRI data yet due to: (1) the varying data quality of physiological recordings, (2) non-standardized peripheral data formats and (3) the lack of full automatization of processing and modeling physiology, required for large-cohort studies.
New methods: We introduce the PhysIO Toolbox for preprocessing of physiological recordings and model-based noise correction. It implements a variety of noise models, such as RETROICOR, respiratory volume per time and heart rate variability responses (RVT/HRV). The toolbox covers all intermediate steps – from flexible read-in of data formats to GLM regressor/contrast creation – without any manual intervention.
Results: We demonstrate the workflow of the toolbox and its functionality for datasets from different vendors, recording devices, field strengths and subject populations. Automatization of physiological noise correction and performance evaluation are reported in a group study (N = 35).

∗ Corresponding author at Translational Neuromodeling Unit (TNU), Institute for Biomedical Engineering, University of Zurich and ETH Zurich, Wilfriedstrasse 6, 8032 Zurich, Switzerland.
E-mail address: kasper@biomed.ee.ethz.ch (L. Kasper).

Comparison with existing methods: The PhysIO Toolbox reproduces physiological noise patterns and correction efficacy of previously implemented noise models. It increases modeling robustness by outperforming vendor-provided peak detection methods for physiological cycles. Finally, the toolbox offers an integrated framework with full automatization, including performance monitoring, and flexibility with respect to the input data.

Conclusions: Through its platform-independent Matlab implementation, open-source distribution, and modular structure, the PhysIO Toolbox renders physiological noise correction an accessible preprocessing step for fMRI data.

1. Introduction

Physiological noise is a major confound for functional magnetic resonance imaging (fMRI), as it perturbs blood-oxygen level dependent contrast (BOLD) by fluctuations of non-neuronal origin (Hutton et al., 2011; Krüger and Glover, 2001; Triantafyllou et al., 2005). The resulting extra variance in the data reduces statistical sensitivity, leading to false negative results. False positives may arise as well, if physiological fluctuations correlate with task components. On top, resting state fMRI analyses suffer from spatial correlations of physiological noise, which create spurious accounts of functional connectivity (Birn, 2012).

The two primary sources of physiological noise are the cardiac and respiratory cycle, which induce signal changes in fMRI time series via the following mechanisms, among others (see (Murphy et al., 2013) for a comprehensive overview). With regard to the cardiac cycle, the blood volume increases in the brain during systole, following the arterial pulse wave and subsequent vessel dilation. This, in turn, leads to displacement and pulsatile flow of the cerebrospinal fluid (CSF) from the ventricles through the aqueduct into the spinal canal (Soellinger, 2008). Likewise, during diastole, blood volume and vessel diameter decrease, while CSF flow is reversed from the spinal tract into the ventricle voids. Moreover, heart-rate variability and blood pressure changes alter blood oxygen level, and thus local T_2^* values (Chang et al., 2009).

The respiratory cycle, on the other hand, induces signal fluctuations in two ways: Firstly, changes in respiratory volume per time alter the concentration of blood CO_2, which is a vasodilator (Birn et al., 2006). Secondly, the bulk motion of magnetized material in the chest induces background magnetic field changes by up to a few Hz between inhalation and exhalation, leading to sub-voxel shifts in echo-planar image encoding (Windischberger et al., 2002).

Interactions of cardiac and respiratory cycle induce further physiological fluctuations, e.g. through the respiratory sinus arrhythmia, i.e. the increased heart rate during inhalation compared to exhalation (Hirsch and Bishop, 1981).

Given these clear mechanisms stemming from only two sources, correction techniques for physiological noise have focused on identifying and removing the characteristics of cardiac and respiratory cycles from fMRI data. Consequently, two distinct approaches have emerged, relying either on intrinsic noise-like properties of the fMRI data ("data-driven"), or on independent external measures of physiology and specific models of their influence on BOLD signals ("model-based").

Concerning data-driven methods, simple temporal filtering of fundamental physiological frequencies is often impossible in fMRI, due to the long repetition time leading to under-sampling and aliasing of physiological signals (but see, for example, (Zahneisen et al., 2014) for fast acquisition techniques and (Tong and Frederick, 2014) for an application to questions regarding physiological noise). However, noise component classification has been demonstrated using principal and independent component analysis, as well as canonical (auto)correlation analysis (PCA, ICA, CCA). Herein,

classifying an identified component as "noise" remains the key challenge, and often requires manual intervention by the operator (e.g. in FSL MELODIC). Automated methods often rely on spatio-temporal priors for the noise, stemming from the aforementioned mechanisms of physiological noise generation. These priors incorporate the temporal dynamics of physiological fluctuations, e.g. heart and breathing rate (spatial ICA, (Thomas et al., 2002)), or their spatial location, e.g. proximity to vessels or ventricles (CORSICA, (Perlbarg et al., 2007), masked ICA (Beissner et al., 2014), CompCor (Behzadi et al., 2007)), or both, (PHYCAA+, Churchill and Strother, 2013). Recently, dictionary-based techniques have gained some attention, alleviating the need for individual subjective component classification through group priors on components (FIX, Salimi-Khorshidi et al., 2014). For studies with multiple runs, instead of noise classification, test-retest reliability of the signal of interest can be employed via cross-validation (Churchill et al., 2012; Kay et al., 2013).

Model-based physiological noise correction, on the other hand, aims at modeling the different mediating mechanisms of voxel-wise fluctuations directly from peripheral recordings of the cardiac and respiratory cycle, using electrocardiograms or photo-plethysmographic units (PPU) and breathing belt measurements, respectively. In particular, the periodic effects of pulsatile motion and field fluctuations can be modelled via a Fourier expansion of physiological phases (RETROICOR, (Glover et al., 2000; Josephs et al., 1997)). End-tidal CO_2 changes and heart-rate dependent blood oxygenation are better approximated by respiratory and cardiac response functions to respiratory volume per time and heart rate variability, respectively (Birn et al., 2008, 2006; Chang et al., 2009; Chang and Glover, 2009). Also, more complex non-linear models from peripheral data exist, such as Bayesian state space models of BOLD and physiological noise (Särkkä et al., 2012). In principle, model-based approaches are capable of a mechanistic and comprehensive physiological noise correction, and promising benefits have been reported, e.g. de-noising high-field or brainstem fMRI data by up to 50% (Brooks et al., 2013; Hutton et al., 2011), as well as removing spurious connectivity in resting-state data (Birn, 2012).

Given the well-established impact of physiological noise on the sensitivity of fMRI analyses, it is somewhat surprising that, to date, only a relatively small fraction of cognitive neuroimaging studies have reported use of physiological noise correction, in particular for task-based fMRI. This is particularly remarkable, given that several freely available implementations of noise correction procedures exist (e.g. to name but a few, AFNI 3DRETROICOR, FSL Physiological Noise Modeling (PNM, Brooks et al., 2008), PhLEM (Verstynen and Deshpande, 2011)). One possible reason is that the available implementations require some degree of intervention by the user (such as manual selection of components, see above), thus aggravating the use of automatic analysis pipelines and impeding the analyses of large datasets. Concerning model-based approaches, a wider adoption of these methods has been hampered by a lack of

automatization with regard to employing the necessary peripheral physiological recordings. Three factors contribute to this situation:

(1) Physiological log-files come in many vendor- and device-dependent custom data formats, which are not interfaced by common noise correction packages.
(2) Peripheral physiological recordings exhibit varying data quality, especially at high fields (e.g. due to the magneto-hydrodynamic effect, which compromises electro-cardiogram (ECG) signals) or in non-compliant subject populations (e.g. motion sensitivity of limb-mounted PPUs), which requires careful scrutiny and preprocessing of the peripheral time series.
(3) Performance evaluation and, thus, quality assurance of the applied correction is not routinely enabled by existing noise modeling approaches, although presented in the accompanying methodological papers, e.g. via standardized reports of additionally explained variance (Brooks et al., 2008; Harvey et al., 2008; Hutton et al., 2011). This assessment, however, is crucial in practice for detecting errors in pipeline-based analyses of larger subject cohorts.

As a consequence, to facilitate the introduction of model-based physiological noise correction to standard fMRI data processing pipelines, an implementation has to fulfill the following specifications, such that manual user interactions and individual programming efforts are minimized:

(1) Flexibility with respect to read-in of various vendor-specific and custom data formats,
(2) Robustness, i.e. reliable preprocessing even of low-quality data, and
(3) Model assessment, i.e. validation of correction efficacy in individual subjects.

In this article, we describe the methodology and implementation of a toolbox that was developed to address these desiderata and support the automatization of model-based physiological noise correction for large group studies. This toolbox called "PhysIO" is distributed under the GNU Public License (GPL 3.0), and is freely available as part of the open source TAPAS software suite (https://www.tnu.ethz.ch/en/software/tapas.html). In short, the toolbox transforms physiological *input*, i.e. peripheral recordings, into physiological *output*, i.e. regressors encoding components of physiological noise, hence the name PhysIO. A modular Matlab implementation supports command-line operation and is compatible with all major fMRI analysis packages via the export of regressor text-files. For the Statistical Parametric Mapping (SPM) software package (www.fil.ion.ucl.ac.uk/spm) in particular, PhysIO features a full integration as a Batch Editor Tool, which allows user-friendly, GUI-based setup and inclusion into existing preprocessing and modeling pipelines.

This paper introduces the modules of the toolbox and typical usage examples, demonstrating flexibility, robustness and quantitative assessment of noise correction for datasets of various origin and quality. These examples serve to illustrate the degree of accomplished automatization of model-based physiological noise correction and are also available for download.

2. Methods

2.1. Overview

This section introduces the modules of the PhysIO Toolbox and its general workflow, as depicted in Fig. 1. Briefly, the peripheral physiological recordings are read in, synchronized to the
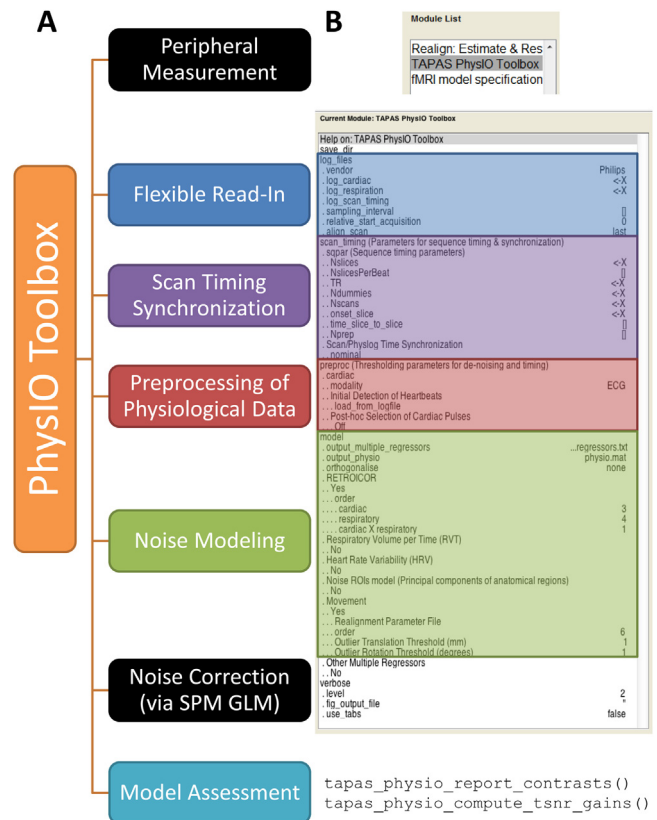
Fig. 1. Workflow of the PhysIO Toolbox. (A) The different modules of the Toolbox in processing order. (B) SPM12 Batch Editor interface of the toolbox; parameters color-coded according to corresponding modules.

fMRI acquisition, preprocessed to retrieve meaningful physiological measures (such as cardiac phase), and finally modelled as nuisance regressors. Noise correction is then performed by entering these regressors into a general linear model (GLM) of fMRI data and can be assessed by the performance evaluation tools of PhysIO (Fig. 1A). Custom regressors (e.g., for spike censoring) can be flexibly derived and added.

This structure is parallelled by the GUI interface of the toolbox within the SPM Batch Editor, which allows for full integration into existing fMRI preprocessing and modeling pipelines (Fig 1B). Note, however, that PhysIO also works as a standalone Matlab toolbox. Each module offers multiple processing options, which are described in the following sections (see also Fig. 2). For concrete settings and parameter names in the modules, see the Supplementary material.

2.2. Example datasets

To show the flexibility and robustness of the toolbox, we demonstrate its application to four datasets (three single subjects, one group dataset) from previously conducted studies. These data were acquired with scanners from different vendors, at different magnetic field strengths and using various peripheral devices. More detail on scan parameters and the image preprocessing of each dataset is provided in Table 1.

(1) Siemens 3T (ECG)

ECG data were recorded as part of an fMRI study on a Siemens Trio 3 T MRI scanner (Garbusow et al., 2016). A 4-electrode ECG recorded the cardiac cycle during the fMRI sessions.

(2) Philips 7T (ECG + Breathing Belt)

ECG and respiratory data were acquired during fMRI using a Philips Achieva 7T system, equipped with a 16-channel head coil.
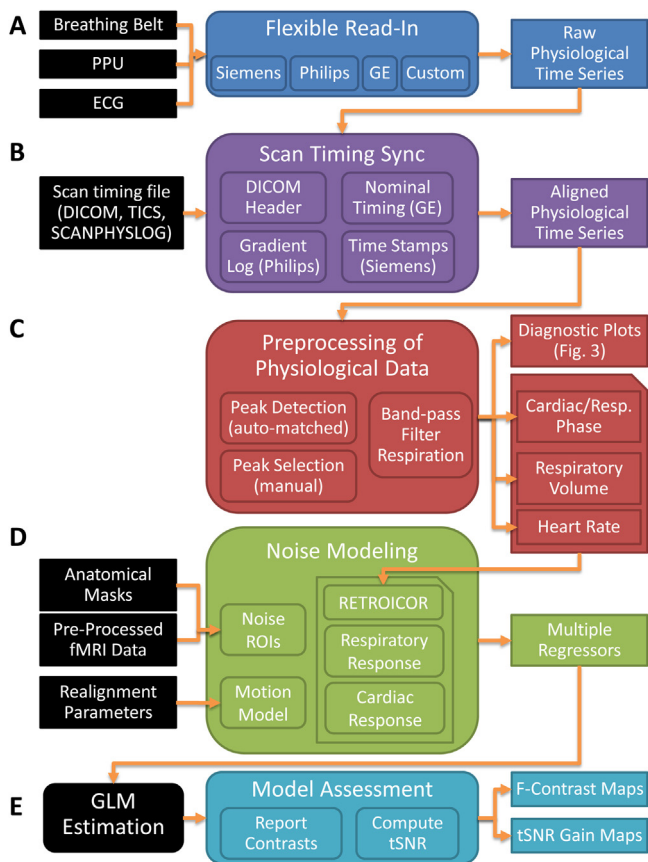
Fig. 2. Detailed flowchart of noise correction via the PhysIO Toolbox. Depicted are the respective inputs (left) to the individual toolbox modules (center), the correspondent outputs (right), and the dependencies between the modules (orange arrows). The toolbox is flexible in terms of peripheral recording devices and physiological data vendor formats (A), realizes synchronization of fMRI and peripheral data (B), provides robust means for preprocessing of corrupted recordings (C), and a variety of established physiological noise models (D), as well as tools for automatic model assessment (E). (For interpretation of the references to colour in this figure legend, the reader is referred to the web version of this article.)

4-electrode ECG and a pneumatic belt were employed for physiological monitoring.

(3) General Electric (GE) 3T (PPU + Breathing belt, children)

Cardiac pulse and respiration data were collected on a 3.0 T GE HD.xt whole-body MRI scanner using an 8-channel head coil (Bollmann, 2014), in the context of an attention-deficit/hyperactivity disorder (ADHD) study, from a child of the control group. PPU and pneumatic belt were employed for physiological monitoring during the fMRI sessions.

(4) Philips 3T (ECG + Breathing Belt):

35 healthy male volunteers participated in a social learning study (Diaconescu et al., 2016, 2014). Data was acquired on a Philips Achieva 3T system equipped with an 8-channel head coil. 4-electrode ECG and a pneumatic belt were employed for physiological monitoring.

From the three single-subject datasets, we utilize the peripheral physiological recordings and fMRI data of one session, to show compatibility of the toolbox with different vendors (Fig. 8). Datasets (2) and (3) further illustrate robustness against poor data quality at ultra-high magnetic field (Fig. 3, 7) or in a motion-prone subject population (Fig. 4, 5).

The fourth dataset serves as our standard example throughout the Modeling section (Fig. 6 , see Software note for accompanying code to reproduce the figure insets). fMRI data from the entire

group study (N = 35) will be presented in the Results section to demonstrate the automatization capabilities of the toolbox (Fig. 9).

2.3. Flexible read-in

The PhysIO toolbox supports the read-in of logfiles from various peripheral devices (Fig. 2A), including ECG, pneumatic belts and photoplethysmographic units (PPU). It offers tested interfaces with the physiological file formats of 3 MR scanner vendors (General Electric, Philips, Siemens releases VB and VD, i.e. the new "tics" time stamp format), as well as the read-in of custom log-files. For the latter, ASCII files with one amplitude sample per line have to be specified. The toolbox accepts different sampling rates for each peripheral recording.

2.4. Scan timing synchronization

This module aligns the time series of physiological data to the fMRI volume time series, which typically differ in their sampling rates. Thereby, temporal shifts are avoided that would bias noise modeling later on. Synchronization can be performed using different inputs, such as fMRI scan-timing files (e.g. Siemens DICOM-header or separate volume/slice acquisition trigger tics file), gradient logging (Philips), or simply derived from nominal fMRI scan parameters and manual recording offsets (Fig. 2B). Details on determining thresholding for gradient logging are provided in the toolbox manual (see also Fig. S1).

2.5. Preprocessing of physiological data

2.5.1. Signal features and noise sources
This most critical part of the toolbox recovers physiological measures (cardiac/respiratory phase, heart rate, respiration volume per time) from noisy peripheral recordings (Fig. 2C). Herein, the periodic nature of cardiac and respiratory data is captured by extracting phase time courses. For the respiratory signal, amplitude changes are computed as well.

In practice, both physiological readouts are often compromised by setup imperfections and challenging subject populations. Cardiac recordings mostly exhibit increased noise levels. For voltage-based signals, such as electrocardiograms (ECG), distortions stem from magnetic field gradient changes and, at high field, the magnetohydrodynamic effect (Krug and Rose, 2011; Tenforde, 2005). For PPUs, mounted on extremities, excessive subject movement introduces noise to the recordings. Respiratory measurements, on the other hand, are compromised through complete temporary signal losses, if pneumatic devices get detached from the subject (zero signal), or are strapped too tightly (signal clipping). Again, subject movement increases readout noise here.

Phase data can in principle be recovered from noisy data via robust peak detection algorithms, identifying repetitive features of the data (e.g., R-peak occurrence in ECG waves). However, long intervals of signal loss prevent the use of amplitude data for physiological noise modeling. The objective of the preprocessing module is therefore two-fold: First, to recover signal features from noisy data, where possible, via a dedicated peak detection algorithm incorporating physiological assumptions. Second, to detect and discard data snippets which are compromised for noise modeling via diagnostic plots of the physiological signal statistics. This prevents overfitting of noise early on and retains degrees of freedom, i.e. sensitivity, for modeling effects of interest.

2.5.2. Assessment of recording quality and recovery
The toolbox offers a standardized procedure for assessing the data quality of peripheral recordings and their recovery. This procedure is represented by a decision tree which selects the best
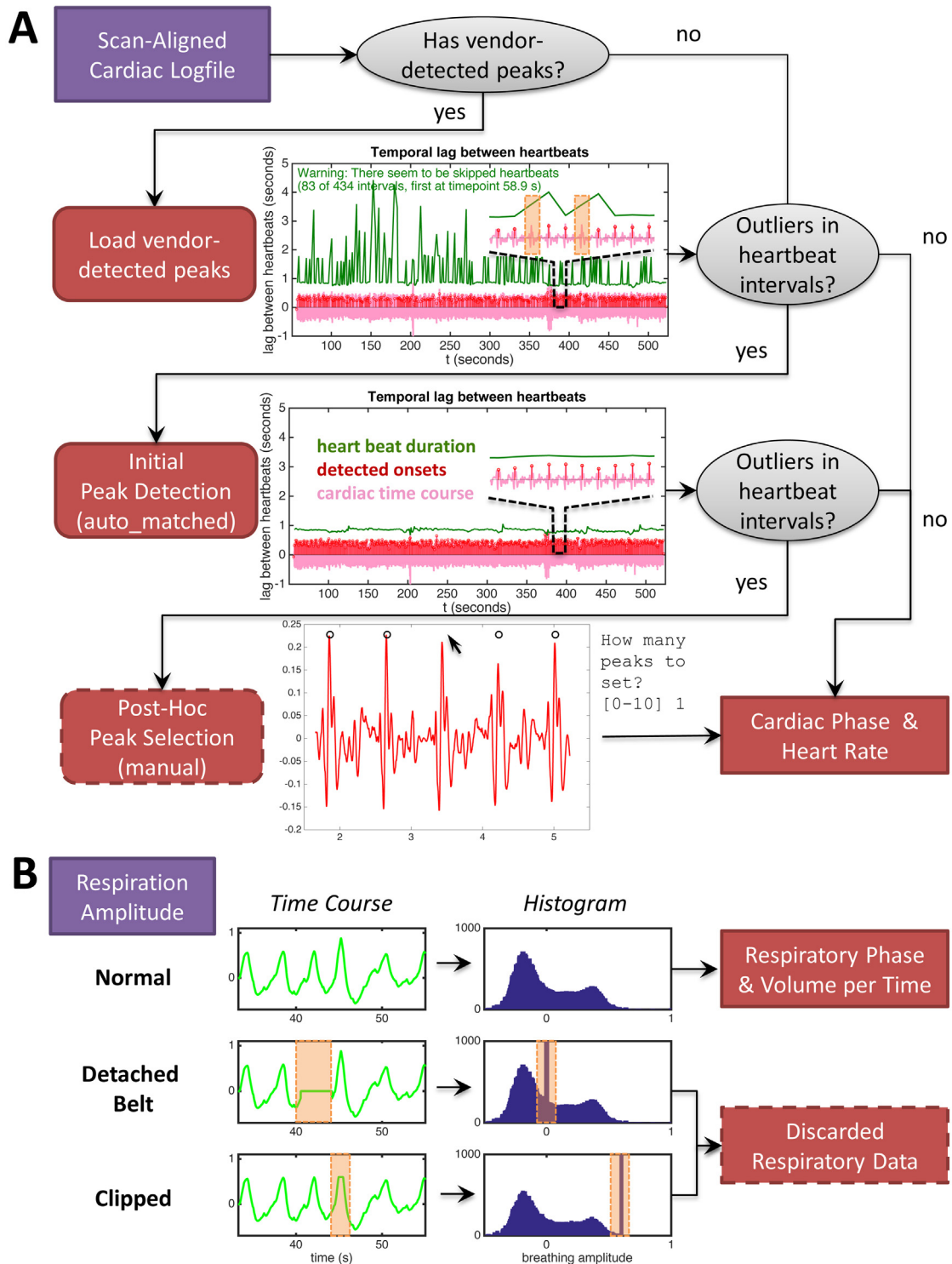
Fig. 3. Preprocessing decision tree (example dataset (2), 7T ECG). The PhysIO Toolbox provides various intermediate outputs to check peripheral recording quality and adjust preprocessing options. (A) The diagnostic plot of the heartbeat interval time course is used as decision criterion for successful cardiac cycle peak detection. Outliers in the heartbeat intervals (green spikes/orange boxes) extracted from prospective vendor triggers ('load_from_logfile') indicate missed or misdetected trigger events, which can be corrected by the matched-template algorithm of PhysIO ('auto_matched'). In rare cases, the algorithm might miss or erroneously detect heartbeat events, which are again reflected as outlier peaks in the diagnostic plot and can be manually corrected (post-hoc correction 'manual') via a GUI, saving selected peaks for reproducibility. (B) Breathing belt amplitude time courses and histograms. (Top) Normal time course and histogram, appropriate for respiratory noise modeling. (Middle) Suspicious histogram peak at 0, indicating a (temporarily) detached belt. (Bottom) Suspicious histogram peak at maximum amplitude, indicating a ceiling effect of respiratory recording (e.g., a too tight belt). For both suspicious histograms, the filtered respiratory time series have to be inspected. Corrupted time windows of constant amplitude are then flagged automatically and can be excluded from later noise modeling. (For interpretation of the references to colour in this figure legend, the reader is referred to the web version of this article.)
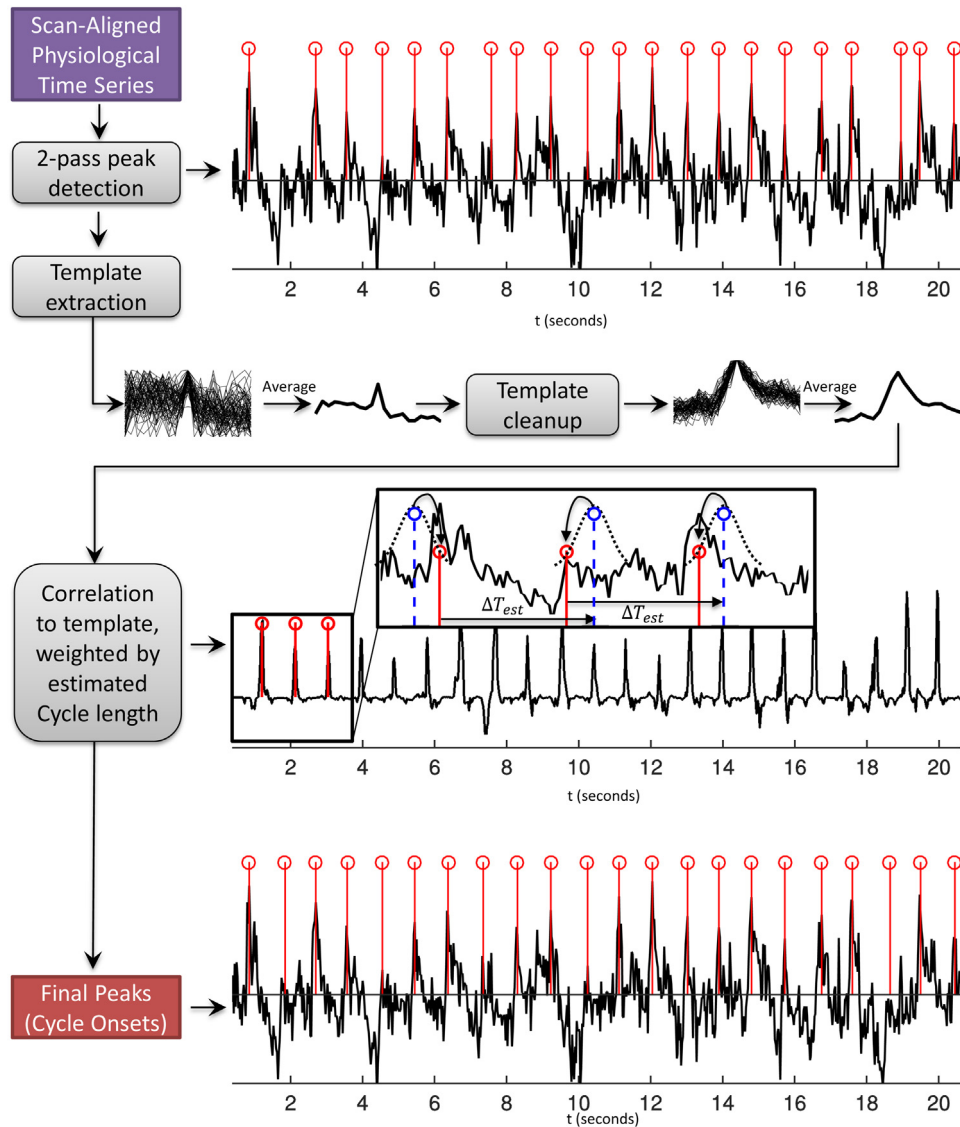
Fig. 4. Physiological Peak Detection Algorithm (example dataset (3), 3T PPU time course of a child). From initial peak detection, an average physiological rate (heart/breathing cycle length) is estimated to inform a second, refined peak detection (top). Discarding outliers, a template of half the physiological cycle surrounding the peaks is created by averaging (middle). Then, an iterative local search is performed to both determine the start phase of the first cycle and detecting all subsequent cycles step-by-step. This algorithm, incorporates prior information on the current cycle length ΔT_{est} to estimate the most likely onset of the next cycle, and penalizes deviations from this starting point by Gaussian discounting (zoomed inset). This prior is combined with measured data by evaluating the correlations to the determined physiological cycle template in the neighborhood of the proposed starting point. The maximum a-posteriori estimate for the cycle onset is selected, and the algorithm continues iteratively to find the next cycle onset. Herein, the cycle length ΔT_{est} for the upcoming cycle is updated online considering the last 20 cycles, accounting e.g. for a variable heart rate or breathing pattern.

preprocessing strategy for cardiac data (Fig. 3A): First, vendor-determined trigger signals might be stored in the physiological logfile alongside the cardiac time course, which can be read in by the toolbox (`load_from_logfile`).

However, vendor-provided peak detection may be incomplete, in particular for noisy peripheral recordings. The vendor algorithms are typically designed to allow real-time triggering of MRI acquisitions. Thus, they are necessarily prospective, deciding on the next peak occurrence relying on the past time series only.

Incomplete peak detection is reflected in a diagnostic plot of the toolbox depicting the time series of heart cycle durations. Unphysiologically short or long heart cycles as well as rapid heart rate changes, are detected by the toolbox, and issue a warning to resort to retrospective peak detection (Fig. 3A). The first – and usually sufficient – stage is an initial peak detection algorithm using data-driven pattern-matching for individual physiological cycles (`auto_matched`), which is explained later

in this section (Fig. 4). Briefly, this algorithm can perform better than prospective detection methods, as it uses knowledge of the whole time series, i.e. past *and* future of a physiological cycle, to detect its onset. As can be seen from the example diagnostic plot in Fig. 3A, the algorithm typically identifies all heartbeat onsets reliably, leaving no outliers in the heartbeat duration time course. In rare cases of remaining outliers, an additional stage of manual peak selection is offered for the affected time windows (`posthoc_cpulse_select = 'manual'`), and user choices are saved for later re-use (option `posthoc_cpulse_select = 'load'`). Finally, if user scrutiny cannot detect cardiac cycles in a significant part of the physiological time series, data from this time window can be flagged and discarded.

For breathing data, the range of preprocessing options is limited, given that the typical problem is not noise, but complete signal loss, for which data dismissal is the only possible consequence. Nev-
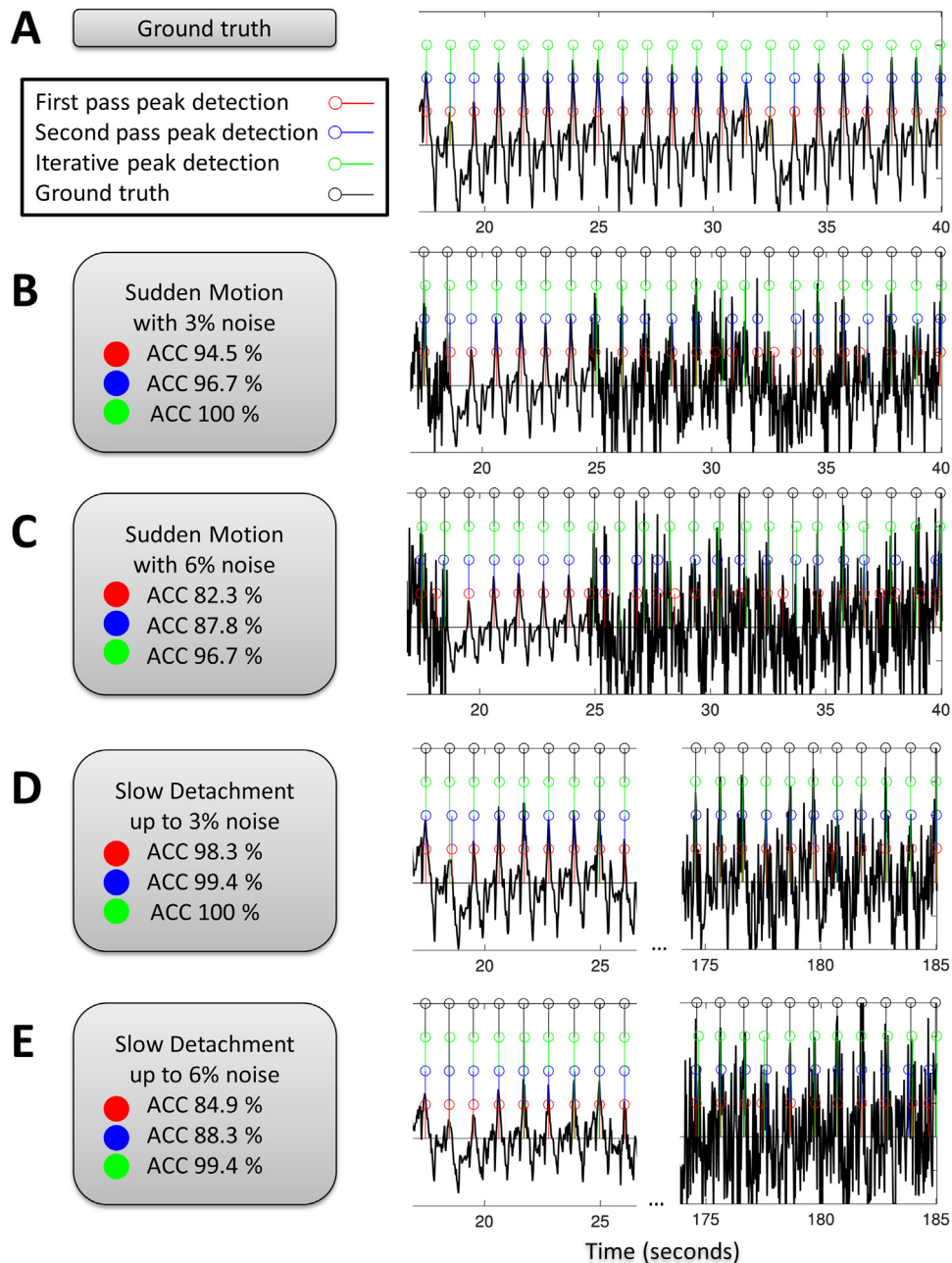
Fig. 5. Simulation-based validation of the template-matching peak detection algorithm. A high-quality ECG signal (A) is perturbed by two types of noise: intermittent Gaussian noise, lasting for a few seconds, mimicking sudden movement confounding recording quality (B,C); and slowly linearly increasing noise, simulating slow detachment of electrodes (or belts) over minutes (D,E). In all cases, the template-based algorithm recovers the ground truth with higher accuracy than simple peak detection (1st pass) or peak detection based on heart rate priors (2nd pass). In particular for cases of higher noise amplitude (C,E), the template-based algorithm outperforms simple peak detection by more than 10 percentage points higher accuracy.

ertheless, the diagnostic plots of the toolbox are still valuable to detect such situations (Fig. 3B). A histogram of the breathing amplitude typically shows a maximum for intermediate amplitudes, with a heavy tail towards high amplitudes, reflecting occasional deep breaths (Fig. 3B, left). If a breathing belt detaches temporarily from the subject, a flat signal is recorded, typically reflected by sharp peaks in the histogram at zero or minimum amplitude (Fig. 3B, middle). Similarly, fixing pneumatic belts too tightly might result in amplitude clipping, i.e., full inhalation exceeding the maximum amplitude of the device's dynamic range. Again, a strong histogram peak at a single value, typically the amplitude maximum, is the consequence.

In case of such unreliable physiological data with long periods of constant signal amplitudes (either due to clipping or detachment), the toolbox will indicate the unreliable time segments of the recording and offers the option to split the subsequent nuisance regressors into a trustworthy and unreliable part (see Section 2.6.3).

2.5.3. Physiological peak detection algorithm

The core preprocessing step for the physiological data is the detection of periodic peaks both in cardiac data (for phase and heart rate) and respiratory data (for respiratory volume estimation, see below and (Birn et al., 2006)). In the PhysIO Toolbox, care has been taken to design the algorithm for specific features of peripheral
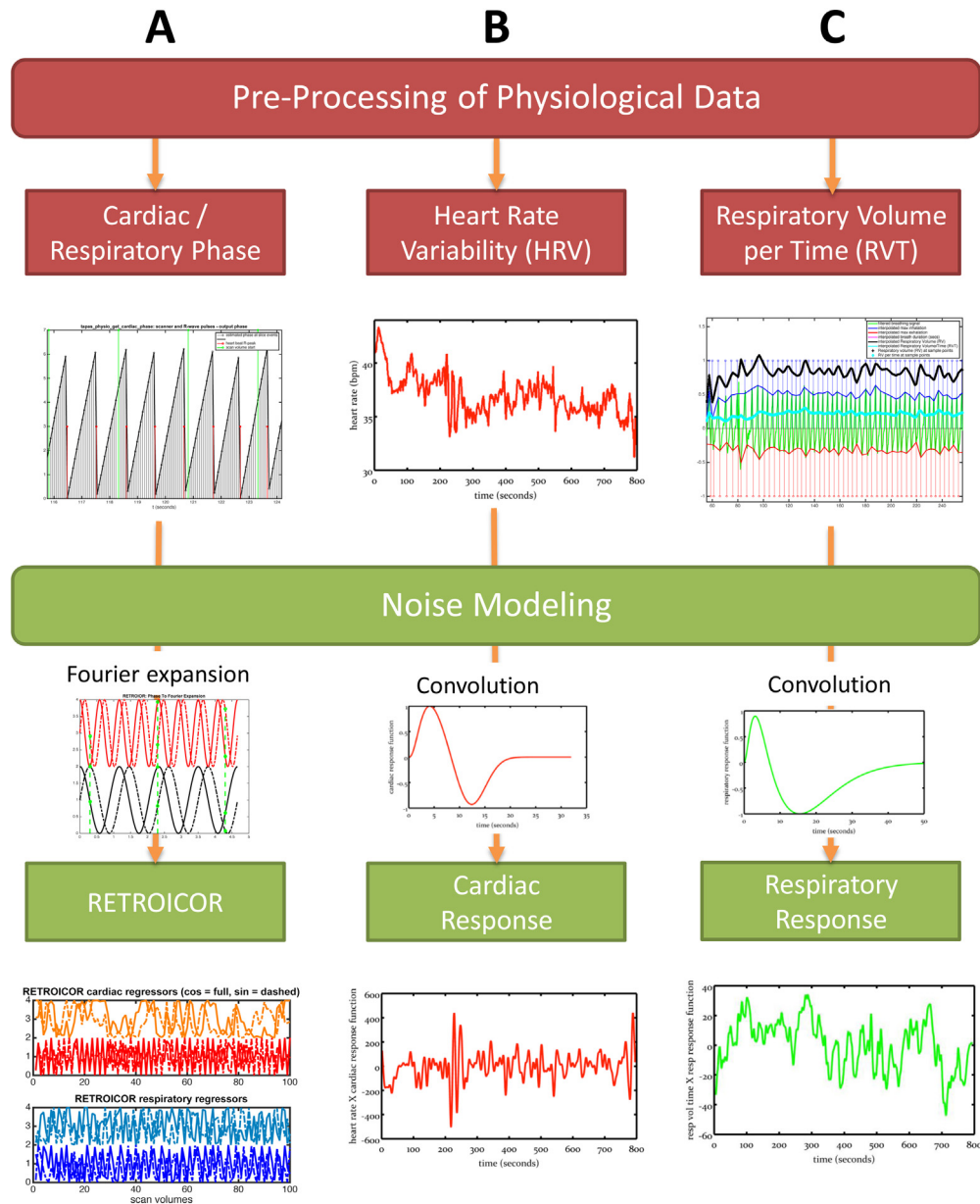
Fig. 6. Physiological Noise Modeling of the PhysIO Toolbox. The preprocessing of peripheral recordings yields physiological determinants (cardiac/respiratory phase, heart rate and respiratory volume per time) at the sampling rate of the peripheral device. From that, RETROICOR regressors are computed via a Fourier expansion (A), whereas cardiac response (B) and respiratory response (C) are calculated by convolution with the cardiac response function (Chang et al., 2009) and respiration response function (Birn et al., 2008), respectively.

data, while keeping it general enough to work robustly for different scan environments, subject populations and recording devices.

Concretely, with respect to the physiological signal, we assume that

1. both cardiac and respiratory data are near-periodic, and
2. changes in heart or breathing rate happen slowly over several cycles.
3. Physiological lower and upper bounds on these rates are expected.
4. No specific shape is assumed for the recurring time course within a physiological cycle (such as an ECG-QRS-wave).
5. Still, we do require some form of prominent peak and that the recurring peak shape remains similar over the whole recording duration.

With respect to the noise encountered in the recordings, we expect that

6. there are extended phases of sufficiently low noise, from which a template of the regular physiological cycle can be extracted.
7. Intervals of higher noise amplitudes are temporary, only lasting a few cycles (or seconds), e.g., due to sudden subject movement.
8. Finally, we assume noise amplitudes to increase during a recording session, i.e., the recording quality to be better at the beginning of the recording than at the end, reflecting, e.g., electrode or belt detachment and declining subject compliance over time.

Based on conditions (1)–(8), the following template-matching algorithm was developed and validated. Violations of the periodicity assumption, e.g. by voluntary changes in breathing amplitude and rhythm, can result in failure of the peak detection, which will issue a warning in case of unphysiological rates and rate changes

(conditions 2 and 3). If such behavior is expected, a less general and more specific algorithm has to be employed, for example, relying on calibration of the expected breathing patterns.

A graphical overview of the template-matching algorithm is provided in Fig. 4; for technical details, please see the function `tapas_physio_get_cardiac_pulses_auto_matched`.

From an initial "first pass" peak detection using a minimum peak height (e.g., 40 percent of the normalized amplitude) and a minimum distance of consecutive peaks (e.g., corresponding to 90 beats per minute), an average heart/breathing rate is estimated (relying on cond. (3) and (5)). This average rate is used in a "second pass", refined peak detection, where the minimum distance of consecutive peaks is constrained to be 80 percent of the average cycle length (Fig. 4, top, relying on cond. (1)-(3)). These settings are reliable defaults in the toolbox which can be adjusted if necessary. A template time course of one physiological cycle is created by averaging all identified cycles, separated by the detected peaks, and cleaned up by removing outliers deviating more than 5 percent from the average template (correlation coefficient < 0.95, relying on condition (4)-(6)). Using maximum correlation to the template, the most representative physiological cycle is determined within the first 20 peaks (relying on cond. (8)). Its peak can be determined most precisely, i.e., with only small phase offset, and serves as an ideal starting point for the iterative peak detection. Therein, a local search propagates backwards to detect all cycles up to the beginning of the recording, i.e., estimate the start phase of the first cycle. In every iteration, the onset of the respective previous cycle is determined by using a Gaussian prior for the peak distance, with the average cycle length (from the first pass peak detection) as its mean and the scaled average cycle length as its standard deviation (relying on cond. (1) and (2)). This prior weights the correlation coefficients of the cycle template with the neighbourhood of every candidate peak (Fig. 4, center, relying on cond. (4) and (5)). After determining the start of the physiological recording in this way, the iterative local search algorithm continues forwards, again iteratively detecting the next cycle via maximum correlation to the determined template and prior information on the current physiological cycle length (Fig. 4, bottom, respecting cond. (5) and (7)). Herein, the average cycle length informing the prior is updated considering only the last 20 cycles, accounting, for example, for a variable heart rate or breathing pattern (respecting cond. (2)). The shape of the template is not updated, assuming deteriorating data quality with increasing recording duration (respecting cond. (8)). The performance of the iterative local search algorithm was tested in a 190s artifact-free 3T ECG dataset where every peak was detected accurately by the simple first pass peak detection. This detection was used as a ground truth, to which two realistic noise patterns were added, each with different noise levels (3 and 6 percent, i.i.d. Gaussian). One pattern resembled periods of sudden motion $(8s \pm 2s)$ with an intermittent increased noise amplitude, while the other mimicked the slow detachment of the recording device, inducing a slow linear drift towards higher noise amplitudes. Performance values of the first and second pass peak detection and the iterative local search algorithm were compared based on detection accuracy and the root mean squared detection time error in relation to the average peak distance (Table 2). The simulations show that the template-matching algorithm, contrary to simple first/second pass peak detection, is indeed capable of recovering the vast majority of cardiac peaks also for both noise patterns and levels, which is reflected in a high accuracy (96.7-100%) and small onset errors (RMS 1.7-4.4% of average heartbeat interval). The test data and peak detection results of the algorithms are illustrated in Fig. 5. In particular for cases of higher noise amplitude (Fig. 5C,E), the accuracy of the template-based algorithm outperforms simple peak detection by more than 10 percentage points.
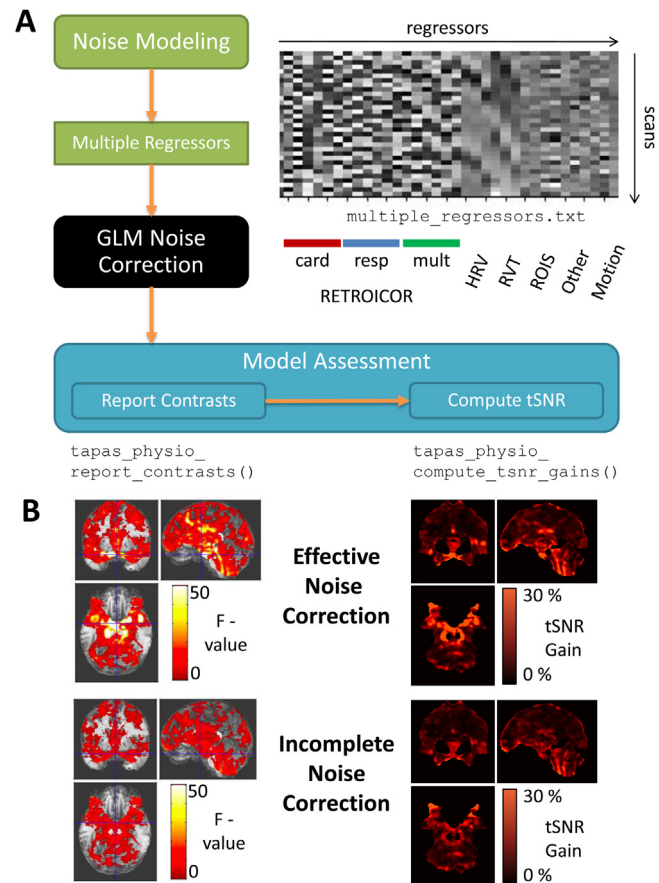
Fig. 7. (A) Performance evaluation of physiological noise modeling. PhysIO outputs a multiple regressors-matrix, combined with movement parameters for e.g. SPM fMRI design specification. After model estimation, the toolbox creates F-contrasts and tSNR maps to assess noise correction and report output figures automatically via different Matlab functions. (B) Example F-contrast and tSNR maps for 7T ECG + breathing belt data set. Effective noise correction (Top row): using preprocessed ECG recordings with iterative template-matched peak detection; Incomplete noise correction (Bottom row): using trigger signal saved in vendor logfile from prospective peak detection. Characteristics of the spatial distribution are less pronounced (F-contrast, left) and the overall efficacy of the noise correction is reduced (tSNR increase through RETROICR correction, right).
[Abbreviations for regressor sets: Card = cardiac, Resp = Respiratory, mult = multiplicative (Card x Resp) interaction of RETROICOR; HRV = Heart Rate Variability; RVT = Respiratory Volume per Time; ROIS = Noise Region of interest mean and principal components; Other = custom-made other regressors from text file; Motion = Motion model from realignment parameters]

2.5.4. Physiological measures: cardiac/respiratory phase, heart rate, and respiratory volume per time

After successful peak detection, quantitative physiological measures can be recovered as inputs for different noise models (Fig. 6, top).

For cardiac models, the phase of the cardiac cycle at each point in the time series is essential, which can be extracted from the onset times of all heartbeats, $t_1, \ldots, t_n, \ldots, t_N$. Concretely, the cardiac phase at time t is expressed as the time passed since the last heartbeat relative to the duration of the current cycle, i.e.

$$\varphi_{card}(t) = 2\pi \frac{t - t_n}{t_{n+1} - t_n} \quad (1)$$

with t_n being the time of the last heartbeat, and t_{n+1} the time of the next one (see Fig. 6A, top, Supplementary material Fig. S2A, and function `tapas_physio_get_cardiac_phase`). Also, the heartbeat onsets yield a direct estimate of the current heart rate $HR(t)$ as the inverse of a sliding window average of heartbeat durations

Table 1
Scan parameters and fMRI preprocessing pipelines of all four example datasets.

Study				
	1	2	3	4
Vendor	*Siemens*	*Philips*	*General Electric*	*Philips*
Field Strength	3 T	7 T	3T	3T
Peripheral Devices	ECG	ECG, Breathing Belt	Pulse Plethysmographic Unit	ECG, Breathing Belt
Scan Parameters				
Sequence	2D EPI	2D EPI	2D EPI	2D EPI
Resolution (mm^3)	$3 \times 3 \times 2$	$1.77 \times 1.77 \times 3$	$3.75 \times 3.75 \times 3$	$2 \times 2 \times 3$
Image Matrix	64×64	124×124	64×64	96×96
Number of Slices	42	36	35	37
Slice Gap (mm)	0	0	0.3	0.6
Flip Angle (deg)	80	70	74	90
TR (ms)	2410	2000	1925	2500
TE (ms)	25	25	32	35
Number of Volumes	462	230	434	1250
Pre-Processing Pipeline				
Software Package	SPM 8, Matlab 2014a, Nipype	SPM 12, Matlab 2015a	SPM 8, Matlab 2012b	SPM 8 (v4385), Matlab 2013a
Step				
1	Slice-Timing Correction	Realign Mean	Realign Mean	Realign Mean
2	Realign 1st	Unified Segmentation	Unified Segmentation	Coregistration EPI to Anatomy
3	EPI Unwarping with B0 maps	Brain Extraction	Brain Extraction	Unified Segmentation
4	Coregistration EPI to Anatomy	Coregistration EPI to Brain	Coregistration EPI to Brain	Normalization EPI (2 mm)
5	Unified Segmentation	Normalization EPI (2 mm)	Normalization EPI (1.5 mm)	Smoothing EPI (6 mm)
6	Normalization EPI (2 mm)	Smoothing EPI (6 mm)	Smoothing EPI (8 mm)	Temporal high-pass filter EPI
7	Smoothing EPI (6 mm)	Temporal high-pass filter EPI	Temporal high-pass filter EPI	
8	Temporal high-pass filter EPI			
List of abbreviations				
Slice-timing Correction	Slice Timing Correction for differences in slice acquisition times with reference to the middle slice			
Realign 1st	Realignment of all EPI volumes to the first			
Realign Mean + Unwarp	Realignment of all EPI volumes to the mean (2-pass), unwarping of motion x B0 interaction			
Realign Mean	Realignment of all EPI volumes to the mean (2-pass)			
Unified Segmentation	Unified segmentation and normalization of the structural MPRAGE/IR-T1-3DTFE image to MNI space			
Brain Extraction	Skull-stripping structural image using tissue probability maps from segmentation			
EPI Unwarping with B0 map	Correction for field inhomogeneities with a voxel displacement map from acquired field maps			
Coregistration EPI to Anatomy	Coregistration of the mean EPI image to the individual structural MPRAGE image			
Coregistration EPI to Brain	Coregistration of the mean EPI image to the skull-stripped structural image			
Normalization EPI (voxel size)	Applying normalization parameters to the EPI images and resampling to new voxel size			
Spatial Smoothing EPI (FWHM size)	Spatial smoothing of the EPI images with a Gaussian kernel of specified full-width-half-maximum.			
Temporal High-pass filter EPI	Temporal high-pass filtering above 1/128 Hz (Part of SPM GLM)			

Table 2
Quantitative assessment of peak detection performance. Three algorithms are compared using measured ECG data with different types and levels of simulated noise: "first pass" = threshold-based peak detection; "second pass" = threshold-based peak detection, using average heartrate from first pass as prior for peak distance; "iterative" = PhysIO algorithm with iterative template-matching and template generation based on the second pass detection ((A) Peak detection accuracy, i.e. relative amount of correctly detected peaks, (detection within 10 samples of the ground truth) (B) Root mean squared error (RMSE) in onset times of detected peaks relative to average heart rate).

A Comparison of peak detection accuracy					
Accuracy in %	Ground truth	Motion + 3 %	Motion + 6 %	Detach + 3 %	Detach + 6 %
First pass	100	94.5	82.3	98.3	84.9
Second pass	100	96.7	87.8	99.4	88.3
Iterative	100	100	96.7	100	99.4

B Comparison of peak detection timing error					
RMSE in %	Ground truth	Motion + 3 %	Motion + 6 %	Detach + 3 %	Detach + 6 %
First pass	0	6.8	11	3.3	9.7
Second pass	0	8.6	14	3	11.7
Iterative	1.7	2.4	4.4	2.2	3.9

(onset differences), where the window length is typically a few TRs, e.g. 6 s (see Fig. 6B, top, Chang et al., 2009; `tapas_physio_hr`).

Respiratory models rely on the phase of the breathing cycle or on respiration volume per time, both computed from an uninterrupted time course of the breathing amplitude (e.g. volume of a pneumatic balloon attached to the chest). The respiratory phase, φ_{resp}, is derived using an equalized-histogram transfer function (Glover et al., 2000), accounting for the differing breathing amplitudes in each cycle (Fig. S2BC, `tapas_physio_get_respiratory_phase`):

$$\varphi_{resp}(t) = \pm\pi \frac{\int_{R_{min}}^{R(t)} H(R)\,dR}{\int_{R_{min}}^{R_{max}} H(R)\,dR} \qquad (2)$$

Here, $R(t)$ is the current amplitude of the respiratory signal and H is the histogram capturing the frequency of each breathing amplitude over the course of the time series. The use of the

histogram-equalization ensures high phase sensitivity at frequent amplitudes. Furthermore, a full breathing cycle is attained only if inhalation and exhalation are both complete. The sign of ϕ_{resp} is determined by the temporal derivative of R, i.e. positive for inhalation ($dR/dt > 0$), and negative for exhalation ($dR/dt < 0$). An estimate of respiratory volume per time (RVT), on the other hand, is retrieved by detecting maximum and minimum peaks in the respiratory time course, computing respiratory volume as difference of subsequent inhalation and exhalation extrema, and dividing it by the temporal spacing of consecutive maxima, i.e. breath duration (see Fig. 6C, top, Birn et al., 2008; `tapas_physio_rvt`). RVT at arbitrary time points is estimated by separate linear interpolation of maxima, minima and breath duration, and computing difference and ratio afterwards.

2.6. Modeling of physiological noise

2.6.1. Noise models of peripheral data: RETROICOR, RVT, HRV

In the fMRI literature on physiological noise, three models informed by peripheral data are particularly prominent (Fig. 6, bottom): RETROICOR phase expansion (Glover et al., 2000; Harvey et al., 2008; Josephs et al., 1997), respiratory volume per time, RVT (Birn et al., 2008), and heart rate variability response, HRV (Chang et al., 2009). These models, which are described in more detail below, are all available within the PhysIO Toolbox (Fig. 2D). Its modular structure also allows for inclusion of custom models (for details, see Supplementary material 8.4). Using any of these models, the toolbox produces regressors which can enter the SPM fMRI model specification directly as confound regressors. As text files, they are also readable outside Matlab/SPM.

In RETROICOR, the periodic effects of pulsatile motion and field fluctuations are modelled as a Fourier expansion of both cardiac and respiratory phase (Fig. 6A, bottom),

$$x_{phys}(t) = \sum_{m=1}^{N_m} A_m \cdot \cos(m\varphi_{phys}(t)) + B_m \cdot \sin(m\varphi_{phys}(t)), \tag{3}$$

where $phys = \{cardiac, respiratory\}$, N_m is the order of the expansion, and A_m, B_m are the Fourier coefficients that have to be estimated for each voxel time series individually. Considering higher harmonics ($N_m > 1$) of the estimated physiological frequencies is a consequence of the low sampling rate of fMRI, typically 0.3-0.5 Hz (TR 2–3s). Thus, aliasing occurs such that the undersampled breathing and cardiac signals (about 0.25 Hz and 1 Hz) fold back into the spectrum of the sampled time series at different frequencies. To account for interaction effects between respiratory and cardiac cycle, e.g. via the respiratory-sinus arrhythmia, extensions to RETROICOR incorporating multiplicative Fourier terms have been proposed (Brooks et al., 2008; Harvey et al., 2008):

$$
\begin{aligned}
x_{cardXresp}(t) = \sum_{m=1}^{N_m} & A_m \cdot \cos\left(m\varphi_{card}(t)\right) \cdot \cos\left(m\varphi_{resp}(t)\right) \\
& + B_m \cdot \sin\left(m\varphi_{card}(t)\right) \cdot \cos\left(m\varphi_{resp}(t)\right) \\
& + C_m \cdot \cos\left(m\varphi_{card}(t)\right) \cdot \sin\left(m\varphi_{resp}(t)\right) \\
& + D_m \cdot \sin\left(m\varphi_{card}(t)\right) \cdot \sin\left(m\varphi_{resp}(t)\right)
\end{aligned}
\tag{4}
$$

In the toolbox, the expansion orders for RETROICOR are freely selectable, with the default following the winning model of (Harvey et al., 2008), i.e., a 3rd order cardiac model (6 regressors, sine/cosine), 4th order respiratory model (8 regressors), and a 1st order interaction model (4 terms).

The respiratory response, as a proxy to end-tidal CO_2 (which impacts on vasodilation), is modelled by convolving the respiratory volume per time (RVT) signal introduced in the previous section,

with a pre-defined respiratory response function $RRF(t)$. In the literature, the RRF was calibrated from BOLD responses to single deep breaths (Birn et al., 2006) under the assumption of a linear-time invariant system (Fig. 6C, bottom). The difference of two gamma variate functions was proposed as parameterization, as is common to describe bolus dynamics. The fit to the experimental data yielded (Birn et al., 2006; `tapas_physio_rrf`):

$$RRF(t) = 0.6t^{2.1}e^{-\frac{t}{1.6}} - 0.0023t^{3.54}e^{-\frac{t}{4.25}} \tag{5}$$

The cardiac response, modeling heart-rate dependent changes of blood oxygenation, is computed as a convolution as well, combining the heart rate variability time course (HRV) with a cardiac response function $CRF(t)$, as suggested in the literature (Fig. 6C, bottom, Chang et al., 2009). The shape of this response function was retrieved from a free-form Gaussian-process deconvolution of experimental BOLD data with respect to the estimated current heart rate. Post-hoc, the resulting CRF was fitted to a combination of a gamma variate and Gaussian function, yielding (Chang et al., 2009; `tapas_physio_crf`):

$$CRF(t) = 0.6t^{2.7}e^{-\frac{t}{1.6}} - \frac{1}{\sqrt{18\pi}}e^{-\frac{(t-12)^2}{4.5}} \tag{6}$$

Since the exact onset time of both cardiac and respiratory response may vary between subjects, the toolbox allows to create multiple shifted versions of the regressors by specifying different delays (as in Bianciardi et al., 2009; Jo et al., 2010).

2.6.2. Data-driven noise models

To facilitate the comparison of peripheral noise models to data-driven methods, we implemented two common approaches, i.e. extended motion modeling and censoring (Friston et al., 1996; Power et al., 2014, 2012), as well as principal component extraction from noise ROIs, based on anatomical priors (aCompCor, Behzadi et al., 2007). The modular structure of the toolbox allows simple extension with further physiological noise models (`physio.model`).

The motion modeling (`model.movement`) relies on pre-estimated realignment parameters (Fig. 2D), which can be used on their own, alongside their computed temporal derivatives, or by inclusion of both sets squared as well, equivalent to a Volterra expansion of the rigid-body motion (Friston et al., 1996). These models are commonly referred to as motion 6/12/24 models, respectively (Siegel et al., 2014). Furthermore, thresholds for maximum translation and rotation between consecutive image volumes can be specified. For volumes exceeding these thresholds, the toolbox creates additional stick regressors (1 for the affected volume, 0 for all others), which absorb any variance from a single motion-compromised volume (motion censoring, (Vergara et al., 2016)).

The anatomical component-based noise extraction (`model.noise_rois`) requires the final preprocessed fMRI data (as nifti or analyze files) as well as anatomical masks (or tissue probability maps e.g. from SPM Segment) of regions assumed to contain noise, but no BOLD signal, e.g. CSF (Fig. 2D). It then extracts the fMRI time series of all included voxels (via SPM) and computes the first principal components, which are output as additional noise regressors, together with the mean time series of the ROI.

2.6.3. Interfacing of other noise modeling and fMRI analysis packages

For inclusion of externally computed nuisance regressors, a sub-module (`model.other`) allows for direct feed-in of ASCII text files, which contain different regressors in columns (separated by white space) and their values per scan volume in rows. These can be combined with regressors computed by any of the methods mentioned above and saved into one common text or Matlab (`.mat`) file (see Fig. 7 for regressor order).
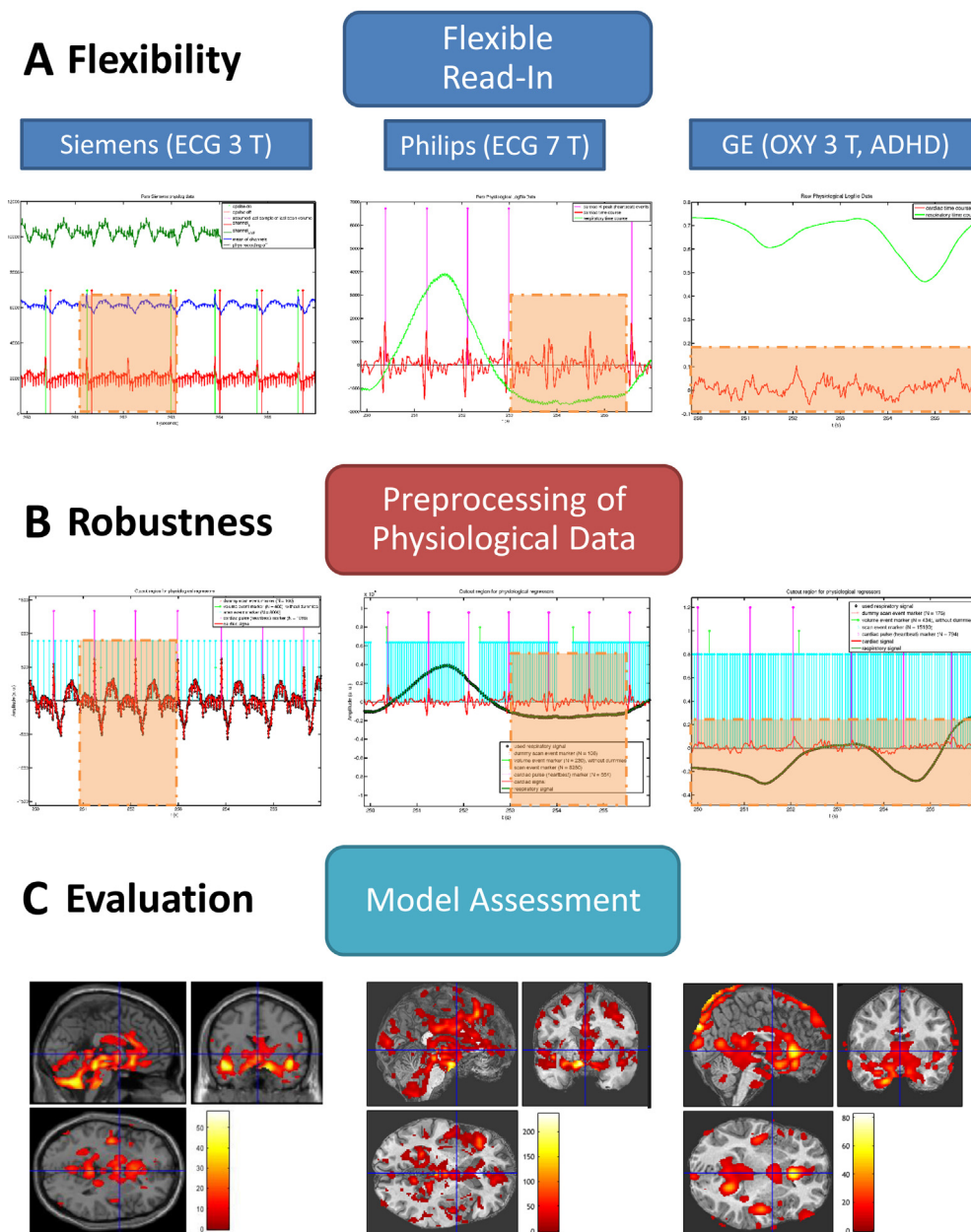
Fig. 8. Flexibility and robustness of preprocessing cardiac data. (A) The toolbox can read vendor log-file data from Siemens, Philips and GE. Note that prospective trigger detection fails occasionally even for 3T ECG data (left) due to causal nature of the filter. At ultra-high field, i.e. 7T, the QRS wave of the ECG is severely distorted, increasing the error rate of missed heartbeats to 19% or more (middle). Prospective peak detection may also fail completely, e.g. for movement-sensitive PPU recordings in children (right). (B) Automatic and reliable detection of heartbeat events was realized by the adaptive 'auto_matched' peak detection algorithm of the PhysIO toolbox (Fig. 4) in all three cases, without user interaction. (C) Model assessment for cardiac RETROICOR regressors via automatic creation and report of the corresponding F-contrasts (p < 0.05 peak-level FWE corrected). The resemblance of the F-maps in terms of major noise sites (insula, ACC, ventricles) confirms successful preprocessing of the peripheral recordings and consistent noise modeling.

Nuisance regressors computed by the above methods have a much higher sampling rate than regressors required for standard general linear model analyses (GLM) of fMRI data that require one value per scan. By default, in our toolbox all regressors are downsampled to a reference slice (for which the models are most accurate), suitable for a single GLM applied to the whole 3D brain volume (as in SPM). Alternatively, slice-specific regressors can be computed by specifying multiple entries of `scan_timing.sqpar.onset_slice`; in this case, individual multiple-regressor text files will be saved, with the respective slice number (indexed by temporal acquisition order) appended to the file name.

If unreliable time segments of physiological recordings have been detected earlier (see section Assessment of Recording Quality and Recovery), the regressors will be split and the common multiple regressors file will contain zeros at these time points. The regressors derived in the unreliable segments are saved in a separate file.

2.7. Noise correction via GLM and inclusion of PhysIO in analysis pipelines

The PhysIO Toolbox leaves the actual correction for the modelled physiological noise to the user's fMRI analysis package of choice. In principle, one could construct and estimate an initial general linear

A

Group-Averaged tSNR Gain

B   **Subject Count with Significant Noise Reduction**
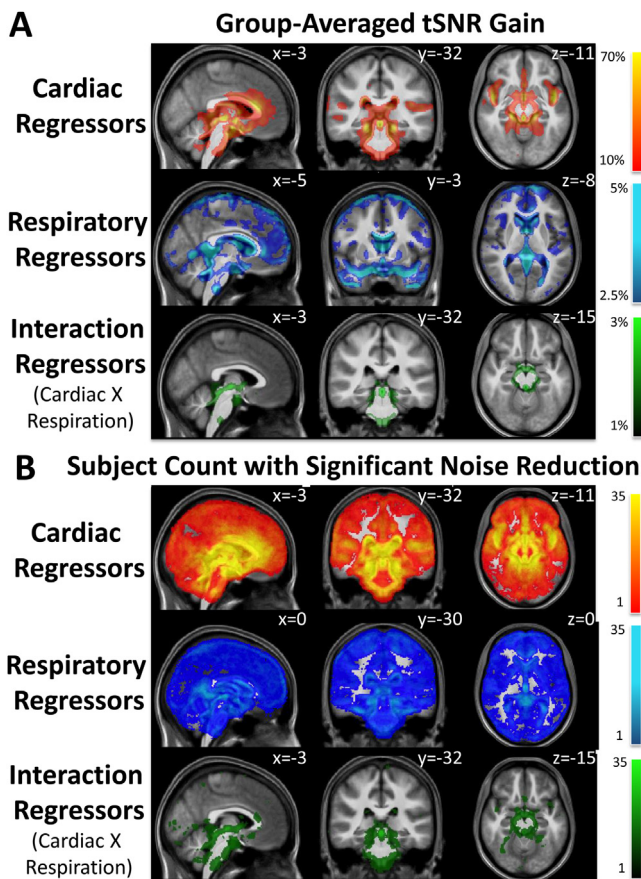
Fig. 9. Automatization of PhysIO usage in an fMRI group study (N = 35, (Diaconescu et al., 2016)). (A) Average tSNR gain map over the entire group. Considerable noise reductions (up to 70%) are realized in the whole group through RETROICOR noise modeling. The prominent areas (brainstem, insula, ACC) match physiological noise sites reported in the literature (Brooks et al., 2013; Hutton et al., 2011). (B) Subject count of significant physiological noise reduction for each voxel in individual 1st level analyses (peak level FWE-corrected p < 0.05). Robustness of the toolbox is confirmed via the high subject count in noise-sensitive areas (cf. (A)). Beyond group results, noise correction for individual subjects can improve sensitivity in all regions of the brain.

model (GLM) containing the created physiological noise regressors only and output the residuals for subsequent analyses in a second GLM. However, we see at least two advantages of a one-step procedure, in which calculated noise regressors are combined with experimental conditions (if applicable) into a single GLM within one of the established software packages. First, statistical inference based on the GLM (e.g., t-tests, F-tests) will have a valid account of the degrees of freedom. Second, in case of correlation between task and noise regressors, shared variance is not attributed to noise exclusively, but can be investigated within the unified GLM.

Practically, providing physiological noise regressors via text files ties in well with established fMRI analysis workflows, since major software packages, like AFNI, FSL and SPM, all allow the inclusion of custom-made nuisance regressors. For example, in SPM, the created text file can be specified as a "multiple regressors" item in the fMRI model specification of the Batch Editor. Due to the tight integration of the PhysIO Toolbox with SPM, the toolbox execution can be specified as a batch item itself, which allows to set all parameters comfortably within the Batch Editor GUI (see Fig. 1). Furthermore, all capabilities of the Batch Editor apply to the toolbox as well, including the specification of dependencies, such that the PhysIO Toolbox can be inserted in a fully automated preprocessing and analysis pipeline (see `example_preproc_physio` in the Supplementary material).

2.8. Model assessment

Finally, following GLM estimation, the toolbox allows to evaluate the performance of physiological noise correction by automatic F-contrast and temporal SNR (tSNR) map generation (Figs. 2 E, 7 A). This is implemented via PhysIO functions interfacing with SPM (`tapas_physio_report_contrasts`, `tapas_physio_compute_tsnr_gains`). The two map types both serve to assess the efficacy of physiological noise correction as well as to review noise preprocessing and data quality. The efficacy of physiological noise correction can be evaluated by comparison with reported effect sizes and sites of physiological noise from the literature (see Fig. 9 as well as Birn et al., 2006; Brooks et al., 2013; Chang and Glover, 2009; Hutton et al., 2011; Jo et al., 2010). If major discrepancies are encountered, the preprocessing of the physiological data should be revisited. Fig. 7B illustrates this situation for the 7T ECG recording (dataset 2), where prospective peak correction, as stored in the logfile, induces less accurate RETROICOR regressors, and thus, less effective noise correction. Both F-maps and tSNR exhibit less of the typical spatial distribution of physiological noise. The concrete manifestation of this incomplete correction, however, will strongly depend on the degree of quality loss in the peripheral recordings. In a worst case scenario, failed recovery of the peripheral recording signal can result in completely ineffective noise correction, reflected in empty F-contrast maps.

F-contrast maps indicate whether sets of regressors (e.g., noise components) explain significant amount of variance collectively, i.e., whether their inclusion in the model is statistically warranted, given the loss of degrees of freedom. In this sense, F-tests perform a nested model comparison (Poline et al., 2007), and are also conceptually very similar to adjusted R^2-values reported in physiological noise literature (Bianciardi et al., 2013; Jo et al., 2010). The PhysIO Toolbox implements the generation of F-contrasts alongside their automatic graphical reporting in a single function, which can be called from the command line (`tapas_physio_report_contrasts`), or via the "Call Function" utility of the SPM Batch Editor. Inputs to the function are a mat-file with the PhysIO-structure and the SPM.mat-file storing the GLM information, to automatically identify relevant regressor groups for contrast generation (such as: RETROICOR cardiac/respiratory/interaction, RVT, HRV, noise ROIs, movement, other – and combinations thereof). Looping over all generated contrasts, the function displays thresholded F-maps as SPM results, overlaid on a pre-specified anatomical image to allow for easier localization of physiological noise sites. All output figures are assembled into a single postscript file, allowing for efficient offline evaluation of the noise modeling performance.

tSNR images are an alternative to F-contrast maps, which are often reported in the physiological noise literature as a sensitivity measure (Brooks et al., 2013; Hutton et al., 2011). They represent the ratio between the average time series signal in a voxel and its standard deviation, i.e., signal fluctuation. Hence, tSNR should increase considerably after physiological noise correction. The ratio of tSNR images after and before correction is equivalent to the reduction factor in standard deviation, and thus closely linked to another common performance measure, the amount of (relative) variance explained (Bianciardi et al., 2013).

The tSNR images are created by a PhysIO toolbox function (`tapas_physio_compute_tsnr_gains`), which can be also be executed within the Batch Editor via the "Call Function" utility. The toolbox makes use of an SPM function (`spm_write_residuals`) to compute residual images of the form

$$Res_n = Y_n - \left(X_{noise} \cdot \boldsymbol{\beta_{noise}}\right)_{\boldsymbol{n}} \tag{7}$$

where n is the scan volume and X_{noise} and $\boldsymbol{\beta_{noise}}$ are the regressor columns and parameter estimates referring to the noise model component in question.

This residual computation also respects the pre-whitening (W) and high-pass filtering (K) matrices incorporated in SPM's GLM estimation procedure, and the Res_n images simply constitute time series de-noised for the targeted noise components, yielding

$$tSNR_{noise-corrected} = \frac{\text{mean}_{n=1...N_{scans}}(Res_n)}{\text{std}_{n=1...N_{scans}}(Res_n)} \quad (8)$$

All tSNR images are saved as nifti-files in the same directory as the SPM.mat, alongside tSNR ratio (or gain) images, divided by the baseline or raw tSNR-image (i.e. without contrast adjustment, only incorporating high-pass filtering and pre-whitening), and can be displayed by any image viewer. For contrasts not originating from the PhysIO Toolbox model itself, tSNR images and ratio images can be computed via the utility function (`tapas_physio_compute_tsnr_spm`).

3. Results

First, we show the flexibility and robustness of the PhysIO Toolbox in preprocessing single-subject data from different vendors, populations and recordings devices (see Table 1 and the Methods section for details of the different datasets). Then, we demonstrate the automatization of noise modeling and performance evaluation enabled by the toolbox for a medium-size group study (N = 35).

3.1. Flexibility & robustness

3.1.1. Single-subject data
Here, we analyze some use cases of the toolbox that illustrate its compatibility with different scanner systems and ranges of data quality. The insets in Fig. 8 are direct output plots of the toolbox that evaluate physiological data and preprocessing quality.

Log-file read-in works for physiological data from three major MR scanner vendors (Siemens, Philips, GE), including ECG and PPU recordings, as well as breathing belt measurements, where applicable (Fig. 8A). Furthermore, pre-determined heartbeat events were read in, as detected by the prospective triggering algorithms of the recording systems. However, the necessity of preprocessing and re-determination of the cardiac cycle was evident for data from all vendors. Even for good recording quality, such as the ECG example acquired on a 3 T Siemens system (Fig. 8A left), prospective heartbeat detection failed occasionally (about 5% misses), and performed prohibitively poorly at ultra-high field (Philips, 7 T, Fig. 8A middle) with 19 % of R-peaks missed in an 8 min session, due to the magnetohydrodynamic effect. Similarly, PPU recordings were compromised in the children population investigated at 3 T, due to increased subject movement (GE 3 T (Bollmann, 2014), Fig. 8A right).

From this visual inspection, as well as following the decision scheme of the toolbox based on its diagnostic plots (Fig. 3A), the automatic peak detection algorithm was applied (Fig. 4). For all three datasets, including the extremely noisy PPU readouts, this algorithm successfully recovered plausible heartbeat onsets, which appear to be complete due to the absence of outliers in the beat duration time course. Consequently, manual peak selection (see Fig. 3) did not have to be invoked in any case. All physiological measures were then synchronized to the timing of the fMRI scans via DICOM header time stamps (Siemens), gradient logging (Philips) or derived from nominal scan parameters (GE) (Fig. 8B, cyan bars indicating slice acquisition onsets).

Finally, the RETROICOR noise model was computed for all three datasets, and model assessment was evoked by an automatic F- contrast report for the group of cardiac regressors (Fig. 8C).

Given the diversity of the underlying fMRI datasets and peripheral recordings, we found good congruence of cardiac noise sites and correction efficacy in the three examples, suggesting consistent model-based physiological noise correction.

3.2. Assessment of recording quality and automatization

In this section, we extend the analysis of the Philips 3T example (ECG + breathing belt (Diaconescu et al., 2016)), which already provided the single-subject example plots for noise modeling (Fig. 6). Here, we apply the toolbox to all 35 subjects included in this study (with 1250 scans per subject) to model physiological noise using RETROICOR for a 3rd order cardiac, 4th order respiratory, and 1st order interaction Fourier expansion of cardiac and respiratory phase (Glover et al., 2000; Harvey et al., 2008). For the corresponding three regressor groups, we present group results of physiological noise correction, namely the tSNR gain maps, averaged over subjects, as well as F-contrast maps (FWE p < 0.05 whole-brain peak-level corrected), summarized by the count of subjects with significant noise correction per voxel in their respective 1st level analyses.

Both the size of noise reduction and its location observed for cardiac and respiratory noise are in line with spatial patterns and tSNR improvements reported in the literature (Harvey et al., 2008; Hutton et al., 2011). The strongest fluctuations correlated to the cardiac cycle (up to 70% tSNR gain, Fig. 9A, top) manifested in the vicinity of major vessels (basilar artery, anterior communicating arteries, internal carotid arteries, sagittal sinus) and in pulsatile CSF regions (especially surrounding the brainstem), but also in some cortical areas involved in interoceptive processes (posterior insula, subgenual ACC; see Discussion). The breathing cycle, on the other hand, induced smaller fluctuations (up to 5% tSNR gain), particularly close to tissue and brain boundaries as well as more inferior brainstem areas, e.g. the pons (Fig. 9A, middle). Interactions between cardiac and respiratory cycle generated additional small noise foci (<3% tSNR gain) in the aqueduct, temporal horn of the lateral ventricle, and the inferior part of the pons, close to the basilar artery (Fig. 9A, bottom).

The map in Fig. 9B shows voxel-wise count of subjects with significant noise correction in their respective 1st level analyses. This confirms that for regions exhibiting prominent physiological noise, as described above, the model-based correction indeed worked for every subject individually. This illustrates the successful automatization of the physiological noise correction and reproducibility across the group. Moreover, it is important to note that noise correction was not only beneficial in these prominent regions, but that nearly every voxel throughout the brain suffered from significant cardiac or respiratory noise in at least one subject (Fig. 9B top and middle). This hints at the importance of model-based physiological noise correction in single-subject analyses, e.g. to enable clinical predictions in individual patients.

4. Discussion

In this paper, we have described the principles, functionality and general workflow of the PhysIO Toolbox for model-based physiological noise correction. We showcased its various applications to task-based fMRI, pointing out its flexibility with regard to both vendor file formats and recording devices, as well as robustness to recording quality. Furthermore, we demonstrated the utility of the toolbox for a fully automated physiological noise correction in the context of group fMRI analysis (N = 35), and illustrated the correction efficacy via the built-in model assessment tools.

The PhysIO Toolbox has so far been downloaded more than 1200 times, as part of the open source TAPAS software collection (www.

translationalneuromodeling.org/tapas). Beyond the data presented here, the PhysIO Toolbox has already been successfully applied to data from several hundred subjects in a number of both task-based and "resting state" fMRI studies (Grueschow et al., 2015; Hauser et al., 2015a, 2015b; Smith-Collins et al., 2015), covering sensory learning paradigms (Iglesias et al., 2013), social learning (Diaconescu et al., 2016), real-time feedback fMRI (Sulzer et al., 2013), high-field fMRI (Kasper et al., 2009), and combinations with other imaging and noise reduction methods, such as EEG or magnetic field monitoring (Hauser et al., 2014; Kasper et al., 2014).

Given the pronounced impact of physiological noise on fMRI signal quality, we envisage that the flexibility and automatization features of the toolbox will be relevant for several areas of application. For example, its flexibility with regard to hardware and data formats renders it attractive for multi-center studies, enabling them to use a single analysis platform despite differences in scanner manufacturers and peripheral devices. The robustness of preprocessing peripheral recordings with the toolbox, in particular cardiac peak detection, will benefit studies involving challenging patient populations, as seen already for ADHD, (Bollmann, 2014), or read-outs of intrinsically poor data quality, such as ECG at ultra-high field (Hutton et al., 2011; Kasper et al., 2009). Additionally, the integrated tools for quality assessment facilitate monitoring of physiological noise correction in large-cohort studies, without the need for prospective quality assessment and pre-selection of peripheral recordings. The platform-independent implementation and modularization of the toolbox allows for fast development and evaluation of new noise correction methods via simple interfaces (see Supplementary material 8.4. for developer notes). Since the toolbox provides high-quality preprocessed physiological measures, more intricate noise models relying on such readouts will particularly benefit (Särkkä et al., 2012). Finally, interfacing on the recording side can be extended easily, as has recently been demonstrated by using NMR field probes for recording cardiac and respiratory cycle simultaneously, to generate RETROICOR regressors with the PhysIO Toolbox (Gross et al., 2015). Currently, the support for file formats from peripheral device vendors is extended, with a native reader for BIOPAC Systems data being already integrated, and support for Brain Products as well Cambridge Electronic Design "Spike" recordings under development.

A question not addressed by this article in detail is the practical utility of physiological noise correction, in terms of sensitivity increases for fMRI analysis. Here, we only reported task-independent tSNR gains, and observed significant noise reductions in the fMRI data through the models implemented by the toolbox. Task-related sensitivity benefits of physiological noise correction have been reported for simple visuo-motor fMRI paradigms (Hutton et al., 2011), and our effect sizes and affected anatomical sites are compatible with these previous findings. We also expect a comparable impact for other cognitive paradigms, foremost in regions which are known to suffer particularly from physiological noise, such as the brainstem (Beissner et al., 2014; Brooks et al., 2013; Vionnet et al., 2015). While a systematic investigation of group level effects of physiological noise correction across cognitive paradigms is still missing, the functionality of the PhysIO toolbox will facilitate such evaluations in the future, and preliminary analyses look promising (Bollmann et al., 2014; Kasper, 2014).

At the single-subject level, the benefits of physiological noise correction for mass-univariate analyses of task-based fMRI data will be three-fold: First, the reduction in residual noise directly enhances the sensitivity for detecting relevant task effects, since both F- and t-values scale inversely with unexplained variance, or its square root, respectively. Second, physiological noise modeling can reduce the risk of false positives and negatives for the contrasts of interest, in case task regressors are partially correlated with physiology. Third, physiological noise modeling removes long-lasting autocorrelation in fMRI voxel time series due to the approximate periodicity of cardiac and respiratory fluctuations, which would otherwise violate AR(1)-assumptions in GLM applications to fMRI data analysis (Kiebel and Holmes, 2007). All these improvements of first-level analyses propagate to the second level (group level), provided that a full mixed effects analysis is performed (Friston et al., 2005; Penny and Holmes, 2007). However, typically, the summary statistics approach is employed in second-level analysis (Holmes and Friston, 1998), where single-subject contrast estimates enter second level analyses. Here, the influence of unexplained variance at the first level on second-level parameter estimates is more complex (Penny and Holmes, 2007) and can sometimes yield surprising results (Mumford and Nichols, 2009). A systematic investigation of this issue for physiological noise correction is, to our knowledge, still outstanding.

While physiological noise clearly represents a confound for most questions and should be corrected for in most fMRI analyses, it should not be applied blindly. Particular care should be taken, for example, in tasks which correlate with changes in cardiac and respiratory processes due to pain or arousal, where physiological noise removal might reduce sensitivity (Jones et al., 2015; Perlaki et al., 2015; Tousignant-Laflamme et al., 2005). In general, physiological noise correction is thus a conservative analysis approach, which prevents false positives at the expense of an increased risk of false negatives in some circumstances. This is a particular issue for studies of interoception (perception of bodily states). In interoceptive tasks, cardiac and respiratory processes become signal sources of interest, and this should be carefully considered in studies focusing, for example, on the insula, a key area of viscerosensory representation (Critchley and Harrison, 2013).

Beyond mass-univariate GLM analyses, physiological noise correction using the PhysIO toolbox can support analyses of both functional connectivity (with regard to either task-based or "resting state" fMRI) and effective connectivity estimated, for example, by dynamic causal modeling (Friston et al., 2005). For functional connectivity analyses, particularly in the "resting state", it is essential to remove physiological noise, as it correlates across brain regions, and can thus be misinterpreted as the neuronally-induced BOLD coupling targeted in resting-state fMRI (Birn, 2012; Cole et al., 2010). For effective connectivity analyses, on the other hand, the modelled time series extracted from brain regions of interest can be adjusted for the PhysIO contrasts. Thereby, unexplained variance of the time series due to physiological fluctuations is reduced and the estimates of relevant connectivity parameters become more robust.

The PhysIO Toolbox models physiological noise based on peripheral cardiac and respiratory recordings. A complimentary approach to modeling physiological noise is to employ refined fMRI data acquisition of considerably higher spatial or temporal resolution. Higher spatial resolution can reduce partial volume effects, i.e., noise bleeding into gray matter from nearby vessels or ventricles, as recently hypothesized and validated for the brainstem (Beissner et al., 2014; Vionnet et al., 2015). High temporal resolution allows, in principle, direct band-pass filtering of physiological signals, provided a sufficiently high sampling rate of cardiac signals (i.e. TR < 0.5 s) is accomplished (Zahneisen et al., 2014). A combined approach achieving both sufficiently high spatial and temporal resolution, however, is not yet available for whole-brain functional MRI, emphasizing the need for noise modeling.

If no peripheral recordings are available, data-driven approaches for noise correction, such as ICA or removal of noise ROI time courses (Behzadi et al., 2007; Salimi-Khorshidi et al., 2014), remain the only alternative. They rely on prior spatio-temporal knowledge, e.g., about the location of physiological noise sites, and require subjective decisions for classification of data into signal and noise components. This is particularly important

considering individual differences in physiological noise expression, presumably in patient populations, but also observed in this work (cf. Fig. 9B). These issues may render data-driven approaches more difficult to validate and less suitable for analysis pipelines of large datasets. One argument in favor of data-driven approaches is that they do not require sufficiently good quality of peripheral recordings. This is a key aspect which the PhysIO Toolbox addresses by means of algorithms for robust preprocessing and quality assessment.

In summary, we have presented the PhysIO Toolbox for automatic preprocessing of peripheral physiological data and model-based physiological noise correction and assessment. The core features of the toolbox are its flexibility, robustness and integrated performance assessment, which allow for automatic operation and direct insertion into fMRI preprocessing pipelines, in particular as an SPM Toolbox via the Batch Editor. We have shown the compatibility of the toolbox with major scanner vendor log-file types and custom formats, allowing for flexible use in multi-center studies using different scanners and peripheral recording hardware, and have demonstrated the utility of the toolbox across a range of recording qualities (e.g. high field, moving patients). Encouraged by its successful application in several studies including hundreds of volunteers, we hope that this open source toolbox will find useful application in future neuroimaging studies of health and disease, particularly in areas strongly affected by physiological noise such as the brainstem (Brooks et al., 2013).

5. Software note

The Matlab code of the PhysIO Toolbox can be downloaded as part of the TAPAS software (https://www.tnu.ethz.ch/en/software/tapas.html), along with further documentation and example datasets (https://www.tnu.ethz.ch/en/software/tapas/data.html). TAPAS will soon become available on GitHub (https://github.com).

Furthermore, all example log-files and scripts to generate the figures presented here are available as Supplementary material to this paper, and can be found on our webpage as well (www.translationalneuromodeling.org/team/lars-kasper).

The primary source of documentation for the PhysIO Toolbox is the constructor function of its core `physio`-structure, `tapas_physio_new`, which lists and documents all PhysIO modules and their individual parameters. A reformatted listing of this constructor is provided in the Supplementary material of this article, as well as specific guidelines how to extend the toolbox with custom noise models.

Acknowledgments

Appendix A. Supplementary data

Supplementary data associated with this article can be found, in the online version, at http://dx.doi.org/10.1016/j.jneumeth.2016.10.019.

References

Behzadi, Y., Restom, K., Liau, J., Liu, T.T., 2007. A component based noise correction method (CompCor) for BOLD and perfusion based fMRI. Neuroimage 37, 90–101, http://dx.doi.org/10.1016/j.neuroimage.2007.04.042.

Beissner, F., Schumann, A., Brunn, F., Eisenträger, D., Bär, K.-J., 2014. Advances in functional magnetic resonance imaging of the human brainstem. Neuroimage 86, 91–98, http://dx.doi.org/10.1016/j.neuroimage.2013.07.081.

Bianciardi, M., Fukunaga, M., van Gelderen, P., Horovitz, S.G., de Zwart, J.A., Shmueli, K., Duyn, J.H., 2009. Sources of functional magnetic resonance imaging signal fluctuations in the human brain at rest: a 7 T study. Magn. Reson. Imaging 27, 1019–1029, http://dx.doi.org/10.1016/j.mri.2009.02.004.

Bianciardi, M., van Gelderen, P., Duyn, J.H., 2013. Investigation of BOLD fMRI resonance frequency shifts and quantitative susceptibility changes at 7 T. Hum. Brain Mapp., http://dx.doi.org/10.1002/hbm.22320, n/a–n/a.

Birn, R.M., Diamond, J.B., Smith, M.A., Bandettini, P.A., 2006. Separating respiratory-variation-related fluctuations from neuronal-activity-related fluctuations in fMRI. Neuroimage 31, 1536–1548, http://dx.doi.org/10.1016/j.neuroimage.2006.02.048.

Birn, R.M., Smith, M.A., Jones, T.B., Bandettini, P.A., 2008. The respiration response function: the temporal dynamics of fMRI signal fluctuations related to changes in respiration. Neuroimage 40, 644–654, http://dx.doi.org/10.1016/j.neuroimage.2007.11.059.

Birn, R.M., 2012. The role of physiological noise in resting-state functional connectivity. Neuroimage 62, 864–870, http://dx.doi.org/10.1016/j.neuroimage.2012.01.016.

Bollmann, S., Kasper, L., Ghisleni, C., Poil, S.-S., Klaver, P., Michels, L., Eich-Höchli, D., Brandeis, D., O'Gorman, R.L., 2014. The impact of physiological artifact correction on task fmri group comparison. In: Proc. Intl. Soc. Mag. Reson. Med. 22, Presented at the ISMRM, 2014, p. 4145.

Bollmann, S., 2014. Multimodal Imaging in Attention-deficit/hyperactivity Disorder (ADHD) (PhD Thesis). ETH Zurich, Zurich.

Brooks, J.C.W., Beckmann, C.F., Miller, K.L., Wise, R.G., Porro, C.A., Tracey, I., Jenkinson, M., 2008. Physiological noise modelling for spinal functional magnetic resonance imaging studies. Neuroimage 39, 680–692, http://dx.doi.org/10.1016/j.neuroimage.2007.09.018.

Brooks, J.C.W., Faull, O.K., Jenkinson, M., 2013. Physiological noise in brainstem fMRI. Front. Hum. Neurosci. 7, 623, http://dx.doi.org/10.3389/fnhum.2013.00623.

Chang, C., Glover, G.H., 2009. Effects of model-based physiological noise correction on default mode network anti-correlations and correlations. Neuroimage 47, 1448–1459, http://dx.doi.org/10.1016/j.neuroimage.2009.05.012.

Chang, C., Cunningham, J.P., Glover, G.H., 2009. Influence of heart rate on the BOLD signal: the cardiac response function. Neuroimage 44, 857–869, http://dx.doi.org/10.1016/j.neuroimage.2008.09.029.

Churchill, N.W., Strother, S.C., 2013. PHYCAA +: An optimized, adaptive procedure for measuring and controlling physiological noise in BOLD fMRI. Neuroimage 82, 306–325, http://dx.doi.org/10.1016/j.neuroimage.2013.05.102.

Churchill, N.W., Yourganov, G., Spring, R., Rasmussen, P.M., Lee, W., Ween, J.E., Strother, S.C., 2012. PHYCAA: Data-driven measurement and removal of physiological noise in BOLD fMRI. Neuroimage 59, 1299–1314, http://dx.doi.org/10.1016/j.neuroimage.2011.08.021.

Cole, D.M., Smith, S.M., Beckmann, C.F., 2010. Advances and pitfalls in the analysis and interpretation of resting-state FMRI data. Front. Syst. Neurosci. 4, 1–15, http://dx.doi.org/10.3389/fnsys.2010.00008.

Critchley, H.D., Harrison, N.A., 2013. Visceral influences on brain and behavior. Neuron 77, 624–638, http://dx.doi.org/10.1016/j.neuron.2013.02.008.

Diaconescu, A.O., Mathys, C., Weber, L.A.E., Daunizeau, J., Kasper, L., Lomakina, E.I., Fehr, E., Stephan, K.E., 2014. Inferring on the Intentions of Others by Hierarchical Bayesian Learning. PLoS Comput. Biol. 10, e1003810, http://dx.doi.org/10.1371/journal.pcbi.1003810.

Diaconescu, A.O., Mathys, C., Weber, L.A.E., Kasper, L., Mauer, J., Stephan, K.E., 2016. Hierarchical Prediction Errors in Midbrain and Septum During Social Learning. Soc. Cogn. Affect. Neurosci., http://dx.doi.org/10.1093/scan/nsw171 (in press).

Friston, K.J., Williams, S., Howard, R., Frackowiak, R.S.J., Turner, R., 1996. Movement-Related effects in fMRI time-series. Magn. Reson. Med. 35, 346–355, http://dx.doi.org/10.1002/mrm.1910350312.

Friston, K.J., Stephan, K.E., Lund, T.E., Morcom, A., Kiebel, S., 2005. Mixed-effects and fMRI studies. Neuroimage 24, 244–252, http://dx.doi.org/10.1016/j.neuroimage.2004.08.055.

Garbusow, M., Schad, D.J., Sebold, M., Friedel, E., Bernhardt, N., Koch, S.P., Steinacher, B., Kathmann, N., Geurts, D.E.M., Sommer, C., Müller, D.K., Nebe, S., Paul, S., Wittchen, H.-U., Zimmermann, U.S., Walter, H., Smolka, M.N., Sterzer, P., Rapp, M.A., Huys, Q.J.M., Schlagenhauf, F., Heinz, A., 2016. Pavlovian-to-instrumental transfer effects in the nucleus accumbens relate to relapse in alcohol dependence. Addict. Biol. 21, 719–731, http://dx.doi.org/10.1111/adb.12243.

Glover, G.H., Li, T.Q., Ress, D., 2000. Image-based method for retrospective correction of physiological motion effects in fMRI: RETROICOR. Magn. Reson. Med. 44, 162–167 (10893535).

Gross, S., Kasper, L., Vionnet, L., Buehrer, M., Pruessmann, K.P., 2015. De-Noising of fMRI time series using NMR field probes for physiology recording. In: Proceedings of the Organization for Human Brain Mapping 21 Presented at the HBM, Honolulu, Hawaii, USA, p. 3728.

Grueschow, M., Polania, R., Hare, T.A., Ruff, C.C., 2015. Automatic versus choice-Dependent value representations in the human brain. Neuron 85, 874–885, http://dx.doi.org/10.1016/j.neuron.2014.12.054.

Harvey, A.K., Pattinson, K.T.S., Brooks, J.C.W., Mayhew, S.D., Jenkinson, M., Wise, R.G., 2008. Brainstem functional magnetic resonance imaging: disentangling signal from physiological noise. J. Magn. Reson. Imaging 28, 1337–1344, http://dx.doi.org/10.1002/jmri.21623.

Hauser, T.U., Iannaccone, R., Ball, J., Mathys, C., Brandeis, D., Walitza, S., Brem, S., 2014. Role of the medial prefrontal cortex in impaired decision making in juvenile attention-deficit/hyperactivity disorder. JAMA Psychiatry 71, 1165–1173, http://dx.doi.org/10.1001/jamapsychiatry.2014.1093.

Hauser, T.U., Hunt, L.T., Iannaccone, R., Walitza, S., Brandeis, D., Brem, S., Dolan, R.J., 2015a. Temporally dissociable contributions of human medial prefrontal subregions to reward-Guided learning. J. Neurosci. 35, 11209–11220, http://dx.doi.org/10.1523/JNEUROSCI.0560-15.2015.

Hauser, T.U., Iannaccone, R., Walitza, S., Brandeis, D., Brem, S., 2015b. Cognitive flexibility in adolescence: neural and behavioral mechanisms of reward prediction error processing in adaptive decision making during development. Neuroimage 104, 347–354, http://dx.doi.org/10.1016/j.neuroimage.2014.09.018.

Hirsch, J.A., Bishop, B., 1981. Respiratory sinus arrhythmia in humans: how breathing pattern modulates heart rate. Am. J. Physiol. 241, H620–629.

Holmes, A., Friston, K., 1998. Generalisability, random effects & population inference. Neuroimage 7, S754.

Hutton, C., Josephs, O., Stadler, J., Featherstone, E., Reid, A., Speck, O., Bernarding, J., Weiskopf, N., 2011. The impact of physiological noise correction on fMRI at 7 T. Neuroimage 57, 101–112, http://dx.doi.org/10.1016/j.neuroimage.2011.04.018.

Iglesias, S., Mathys, C., Brodersen, K.H., Kasper, L., Piccirelli, M., den Ouden, H.E.M., Stephan, K.E., 2013. Hierarchical prediction errors in midbrain and basal forebrain during sensory learning. Neuron 80, 519–530, http://dx.doi.org/10.1016/j.neuron.2013.09.009.

Jo, H.J., Saad, Z.S., Simmons, W.K., Milbury, L.A., Cox, R.W., 2010. Mapping sources of correlation in resting state FMRI, with artifact detection and removal. Neuroimage 52, 571–582, http://dx.doi.org/10.1016/j.neuroimage.2010.04.246.

Jones, C.L., Minati, L., Nagai, Y., Medford, N., Harrison, N.A., Gray, M., Ward, J., Critchley, H.D., 2015. Neuroanatomical substrates for the volitional regulation of heart rate. Front. Psychol., 300, http://dx.doi.org/10.3389/fpsyg.2015.00300.

Josephs, O., Howseman, A.M., Friston, K.J., Turner, R., 1997. Physiological noise modelling for multi-slice EPI fMRI using SPM. In: Proceedings of the 5th Annual Meeting of ISMRM, Presented at the ISMRM, Vancouver, Canada, p. 1682.

Kasper, L., Marti, S., Vannesjo, S.J., Hutton, C., Dolan, R., Weiskopf, N., Stephan, K.E., Prüssmann, K.P., 2009. Cardiac artefact correction for human brainstem fMRI at 7 tesla. In: Proceedings of the Organization for Human Brain Mapping 15, Presented at the HBM, San Francisco, p. 395.

Kasper, L., Haeberlin, M., Dietrich, B.E., Gross, S., Barmet, C., Wilm, B.J., Vannesjo, S.J., Brunner, D.O., Ruff, C.C., Stephan, K.E., Pruessmann, K.P., 2014. Matched-filter acquisition for BOLD fMRI. Neuroimage 100, 145–160, http://dx.doi.org/10.1016/j.neuroimage.2014.05.024.

Kasper, L., 2014. Noise Reduction in fMRI Utilizing Concurrent Magnetic Field Monitoring (PhD Thesis). ETH Zurich, Zurich.

Kay, K., Rokem, A., Winawer, J., Dougherty, R., Wandell, B., 2013. GLMdenoise: a fast, automated technique for denoising task-based fMRI data. Front. Neurosci. 7, 247, http://dx.doi.org/10.3389/fnins.2013.00247.

Kiebel, S.J., Holmes, A.P., 2007. Chapter 8 – the general linear model. In: Karl Friston, John Ashburner, Stefan Kiebel, Thomas Nichols, William PennyA2 Karl Friston, -J.A., William Penny (Eds.), Statistical Parametric Mapping. Academic Press, London, pp. 101–125.

Krüger, G., Glover, G.H., 2001. Physiological noise in oxygenation-sensitive magnetic resonance imaging. Magn. Reson. Med. 46, 631–637, http://dx.doi.org/10.1002/mrm.1240.

Krug, J.W., Rose, G., 2011. Magnetohydrodynamic distortions of the ECG in different MR scanner configurations. In: Computing in Cardiology, 2011, Presented at the Computing in Cardiology, 2011, pp. 769–772.

Mumford, J.A., Nichols, T., 2009. Simple group fMRI modeling and inference. Neuroimage 47, 1469–1475, http://dx.doi.org/10.1016/j.neuroimage.2009.05.034.

Murphy, K., Birn, R.M., Bandettini, P.A., 2013. Resting-state fMRI confounds and cleanup. NeuroImage Mapp. Connectome 80, 349–359, http://dx.doi.org/10.1016/j.neuroimage.2013.04.001.

Penny, W.D., Holmes, A.J., 2007. Chapter 12 – random effects analysi. In: Karl Friston, John Ashburner, Stefan Kiebel, Thomas Nichols, William PennyA2 Karl Friston, -J.A., William Penny (Eds.), Statistical Parametric Mapping. Academic Press, London, pp. 156–165.

Perlaki, G., Orsi, G., Schwarcz, A., Bodi, P., Plozer, E., Biczo, K., Aradi, M., Doczi, T., Komoly, S., Hejjel, L., Kovacs, N., Janszky, J., 2015. Pain-related autonomic response is modulated by the medial prefrontal cortex: an ECG–fMRI study in men. J. Neurol. Sci. 349, 202–208, http://dx.doi.org/10.1016/j.jns.2015.01.019.

Perlbarg, V., Bellec, P., Anton, J.-L., Pélégrini-Issac, M., Doyon, J., Benali, H., 2007. CORSICA: correction of structured noise in fMRI by automatic identification of ICA components. Magn. Reson. Imaging 25, 35–46, http://dx.doi.org/10.1016/j.mri.2006.09.042.

Poline, J., Kherif, F., Penny, C., Penny, W., 2007. Chapter 9 – contrasts and classical inference. In: Karl Friston, John Ashburner, Stefan Kiebel, Thomas Nichols, William Penny A2 Karl Friston, -J.A., William Penny (Eds.), Statistical Parametric Mapping. Academic Press, London, pp. 126–139.

Power, J.D., Barnes, K.A., Snyder, A.Z., Schlaggar, B.L., Petersen, S.E., 2012. Spurious but systematic correlations in functional connectivity MRI networks arise from subject motion. Neuroimage 59, 2142–2154, http://dx.doi.org/10.1016/j.neuroimage.2011.10.018.

Power, J.D., Mitra, A., Laumann, T.O., Snyder, A.Z., Schlaggar, B.L., Petersen, S.E., 2014. Methods to detect, characterize, and remove motion artifact in resting state fMRI. Neuroimage 84, 320–341, http://dx.doi.org/10.1016/j.neuroimage.2013.08.048.

Särkkä, S., Solin, A., Nummenmaa, A., Vehtari, A., Auranen, T., Vanni, S., Lin, F.-H., 2012. Dynamic retrospective filtering of physiological noise in BOLD fMRI: DRIFTER. Neuroimage 60, 1517–1527, http://dx.doi.org/10.1016/j.neuroimage.2012.01.067.

Salimi-Khorshidi, G., Douaud, G., Beckmann, C.F., Glasser, M.F., Griffanti, L., Smith, S.M., 2014. Automatic denoising of functional MRI data: combining independent component analysis and hierarchical fusion of classifiers. Neuroimage 90, 449–468, http://dx.doi.org/10.1016/j.neuroimage.2013.11.046.

Siegel, J.S., Power, J.D., Dubis, J.W., Vogel, A.C., Church, J.A., Schlaggar, B.L., Petersen, S.E., 2014. Statistical improvements in functional magnetic resonance imaging analyses produced by censoring high-motion data points. Hum. Brain Mapp. 35, 1981–1996, http://dx.doi.org/10.1002/hbm.22307.

Smith-Collins, A.P.R., Luyt, K., Heep, A., Kauppinen, R.A., 2015. High frequency functional brain networks in neonates revealed by rapid acquisition resting state fMRI. Hum. Brain Mapp. 36, 2483–2494, http://dx.doi.org/10.1002/hbm.22786.

Soellinger, M., Assessment of intracranial dynamics using MRI (PhD Thesis), 2008, ETH Zurich, Zurich.

Sulzer, J., Sitaram, R., Blefari, M.L., Kollias, S., Birbaumer, N., Stephan, K.E., Luft, A., Gassert, R., 2013. Neurofeedback-mediated self-regulation of the dopaminergic midbrain. Neuroimage 83, 817–825, http://dx.doi.org/10.1016/j.neuroimage.2013.05.115.

Tenforde, T.S., 2005. Magnetically induced electric fields and currents in the circulatory system. Prog. Biophys. Mol. Biol. 87, 279–288, http://dx.doi.org/10.1016/j.pbiomolbio.2004.08.003.

Thomas, C.G., Harshman, R.A., Menon, R.S., 2002. Noise reduction in BOLD-Based fMRI using component analysis. Neuroimage 17, 1521–1537, http://dx.doi.org/10.1006/nimg.2002.1200.

Tong, Y., de Frederick, B., 2014. Studying the spatial distribution of physiological effects on BOLD signals using ultrafast fMRI. Front. Hum. Neurosci. 8, 196, http://dx.doi.org/10.3389/fnhum.2014.00196.

Tousignant-Laflamme, Y., Rainville, P., Marchand, S., 2005. Establishing a link between heart rate and pain in healthy subjects: a gender effect. J. Pain 6, 341–347, http://dx.doi.org/10.1016/j.jpain.2005.01.351.

Triantafyllou, C., Hoge, R.D., Krueger, G., Wiggins, C.J., Potthast, A., Wiggins, G.C., Wald, L.L., 2005. Comparison of physiological noise at 1.5 T, 3 T and 7 T and optimization of fMRI acquisition parameters. Neuroimage 26, 243–250, http://dx.doi.org/10.1016/j.neuroimage.2005.01.007.

Vergara, V.M., Mayer, A.R., Damaraju, E., Hutchison, K., Calhoun, V.D., 2016. The effect of preprocessing pipelines in subject classification and detection of abnormal resting state functional network connectivity using group ICA. Neuroimage, http://dx.doi.org/10.1016/j.neuroimage.2016.03.038, in press.

Verstynen, T.D., Deshpande, V., 2011. Using pulse oximetry to account for high and low frequency physiological artifacts in the BOLD signal. Neuroimage 55, 1633–1644, http://dx.doi.org/10.1016/j.neuroimage.2010.11.090.

Vionnet, L.M., Kasper, L., Wyss, M., Bruegger, M., Pruessmann, K.P., 2015. Investigation of physiological noise in brainstem fMRI at high resolution. In: Proc Intl. Soc. Mag. Reson. Med. 23, Toronto, Canada, p. 2286.

Windischberger, C., Langenberger, H., Sycha, T., Tschernko, E.M., Fuchsjäger-Mayerl, G., Schmetterer, L., Moser, E., 2002. On the origin of respiratory artifacts in BOLD-EPI of the human brain. Magn. Reson. Imaging 20, 575–582, http://dx.doi.org/10.1016/S0730-725X(02)00563-5.

Zahneisen, B., Assländer, J., LeVan, P., Hugger, T., Reisert, M., Ernst, T., Hennig, J., 2014. Quantification and correction of respiration induced dynamic field map changes in fMRI using 3D single shot techniques. Magn. Reson. Med. 71, 1093–1102, http://dx.doi.org/10.1002/mrm.24771.